Key Points:
- The stratification in the upper and lower bays is mainly controlled by longitudinal wind straining and lateral wind straining, respectively
- Axial winds change tidal asymmetries in stratification and cause wind-induced sediment pumping
- Up-estuary wind enhances seaward sediment transport whereas down-estuary has mild effect

Correspondence to:
W. Gong,
gongwp@mail.sysu.edu.cn

Axial Wind Effects on Stratification and Longitudinal Sediment Transport in a Convergent Estuary During Wet Season

Lianghong Chen[1,2], **Wenping Gong**[1,2,3] (ID), **Malcom E. Scully**[4] (ID), **Heng Zhang**[1,2,3], **Weicong Cheng**[1,2], and **Wei Li**[1]

[1]School of Marine Sciences, Sun Yat-sen University, Guangzhou, China, [2]Southern Marine Science and Engineering Guangdong Laboratory, Zhuhai, China, [3]Guangdong Provincial Key Laboratory of Marine Resources and Coastal Engineering, Guangzhou, China, [4]Applied Ocean Physics and Engineering, Woods Hole Oceanographic Institution, Woods Hole, MA, USA

Abstract The Coupled Ocean-Atmosphere-Wave-Sediment Transport (COAWST) modeling system was used to examine axial wind effects on vertical stratification and sediment transport in a convergent estuary. The model demonstrated that stratification dynamics in the upper estuary (Kelvin number <1; $Ke = \frac{fB}{\sqrt{g'h_s}}$) are dominated by longitudinal wind straining, whereas the dominant mechanism governing estuarine stratification in the lower estuary (Kelvin number ~1) is lateral wind straining. Barotropic advection contributes to seaward sediment transport and peaks during spring tides, whereas estuarine circulation causes landward sediment transport with a maximum during neap tides. Down-estuary winds impose no obvious effects on longitudinal sediment flux, whereas up-estuary winds contribute to enhanced seaward sediment flux by increasing the tidal oscillatory flux. The model also demonstrates that bottom friction is significantly influenced by vertical stratification over channel regions, which is indirectly affected by axial winds.

Plain Language Summary Winds have significant impacts on estuarine density stratification and sediment dynamics, which may affect water quality, siltation of navigation channels, and the overall health of estuarine ecosystems. Despite this great influence, the mechanisms controlling stratification and sediment transport by axial winds in a convergent estuary have not received adequate attention. Here we use a coupled ocean model system to examine axial wind effects on vertical stratification and sediment transport in a convergent estuary. The ocean model reproduced the observed water elevation, velocity, salinity, and sediment concentration well and shows that the density stratification in the upper bay is mainly controlled by longitudinal wind straining, whereas that in the lower bay is dominated by lateral wind straining. Up-estuary wind enhances seaward sediment transport by increasing the tidal oscillatory flux, whereas down-estuary wind has a limited effect. Through this study we advanced our understanding on stratification and sediment transport in a convergent estuary and noted that winds have great influence on tidal oscillatory sediment transport, which may change the sedimentary budget in an estuary.

1. Introduction

Sediment dynamics in estuaries have significant impacts on water quality, siltation of navigation channels, erosion and accretion of tidal wetlands, and the overall health of estuarine ecosystems. Thus, understanding sediment dynamics is of considerable ecological and economical importance. Sediment transport is modulated by a variety of physical processes, including tides, river discharge (Allen et al., 1980; Gong et al., 2014), winds (Chen & Sanford, 2009a), baroclinic circulation (Meade, 1969; Wei et al., 2018), Earth's rotation (Huijts et al., 2006; Schulz et al., 2017), waves (George et al., 2018; Hoefel, 2003), geometry and bathymetry (Ralston et al., 2012; Kumar et al., 2017), tidal asymmetries in mixing (Scully & Friedrichs, 2007a, 2007b; Sommerfield & Wong, 2011; Gong et al., 2016), and settling and erosion lags (Cheng & Wilson, 2008; Chernetsky et al., 2010). The effects of river discharge, tides, and waves on sediment dynamics have been intensively studied. In contrast, relatively few studies have addressed the influence of axial winds on sediment dynamics, except that by Chen and Sanford (2009a), which focused on the axial wind effect in a straight estuary. Most studies that have included wind forcing on sediment dynamics have focused on

wind-induced resuspension of sediment from tidal flats and shallow coastal estuaries (de Jorge & van Beusekom, 1995; Whipple et al., 2018).

Wind effects on hydrodynamics have been intensively studied, including the role of wind forcing in controlling estuarine stratification (Scully et al., 2005; Chen & Sanford, 2009a; Li & Li, 2011; Xie & Li, 2018), lateral circulation (Sanford et al., 1990; Scully, 2010; Scully et al., 2009), direct wind-driven mixing (Chen and Sanford, 2009), and wind-driven waves (George et al., 2018). Scully et al. (2005) presented a simple conceptual model for wind straining, in which down-estuary winds enhance the tidally averaged vertical shear, interacting with the along-channel density gradient to increase vertical stratification, whereas up-estuary winds tend to reduce or even reverse the vertical shear, reducing vertical stratification. Chen and Sanford (2009) showed that stratification is largely modulated by the competition between wind straining and direct wind-driven mixing. Li and Li (2011) suggested that wind-driven lateral straining may partially offset longitudinal straining, causing an asymmetry in modulating stratification between the down-estuary and up-estuary winds. Xie and Li (2018) clarified the effects of wind straining on estuarine stratification and suggested that the cross-channel straining played a dominant role in altering stratification in the lower part of the Chesapeake Bay.

Lateral circulation can play an important role in estuarine sediment dynamics. Although the strength of a lateral current is generally 10% of the strength of the along-channel flow, the magnitude of cross-channel advective terms in the longitudinal momentum and tracer equations is often as large or larger than the respective along-channel counterparts because lateral gradients in velocity, salinity, turbidity, and other tracers are often larger than their respective along-channel gradients (Chant, 2007). A number of mechanisms drive lateral flows, including differential advection (Huijts et al., 2009; Huijts et al., 2011; Lerczak & Rockwell Geyer, 2004; Nunes & Simpson, 1985), Ekman forcing (Cheng et al., 2017; Huijts et al., 2006), diffusive boundary layers (Garrett et al., 1993), cross-stream density gradients (Scully et al., 2009; Chen & Sanford, 2009a), and channel curvature (Chant, 2002). Li and Li (2012) showed that wind-driven lateral circulation causes an asymmetric baroclinic forcing between up- and down-estuary winds and plays an important role in the longitudinal flow.

Huijts et al. (2006, 2009, 2011) used an idealized model to explore lateral residual flows in tidal estuaries and investigate their role in lateral sediment trapping. Their results demonstrated that lateral circulation favors the trapping of suspended sediment on the left shoal of an estuarine channel (looking landward in the Northern Hemisphere). However, the picture of wind-driven lateral flow in a convergent estuary has not received adequate attention, and thus, their solution is incomplete.

To address this gap, we used a state-of-the-art coupled numerical modeling system to investigate the response of hydrodynamics and sediment dynamics to different axial winds in a convergent estuary. Our main objectives were to (1) reveal the effect of axial winds on vertical stratification in the convergent estuary and examine the relative importance of longitudinal and lateral wind straining and (2) explore how axial winds influence suspended sediment dynamics, including bottom stress and sediment transport.

The structure of this paper is as follows. Section 2 presents a description of the study area, followed by a brief introduction of how we implement model simulations (section 3). Using the validated model, we investigate the changes in estuarine circulation, salinity, and sediment dynamics caused by up- and down-estuary winds (section 4). To unveil the bathymetric effects of the convergent estuary, we analyze the change in vertical stratification through diagnostic model studies at the upper and lower estuary. Section 5 presents the analysis of wind effects on the suspended sediment transport and the intrinsic connection between vertical stratification and sediment flux. Finally, conclusions are drawn in section 6.

2. Study Area

The study was conducted in the Huangmaohai Estuary (HE), located in the southwest of the Pearl River Delta (PRD), China (Figure 1a). The HE exhibits convergent geometry, with the width of the estuary narrowing from 35 km at the mouth to 1.9 km at the confluence of the Hutiaomen (HTM) outlet and the Yamen (YM) outlet (Gong et al., 2016). At the estuary mouth, a chain of rocky islands, including Dajin, Hebao, and Gaolan Islands, impede offshore wave propagation into the estuary. Note that this study neglects the
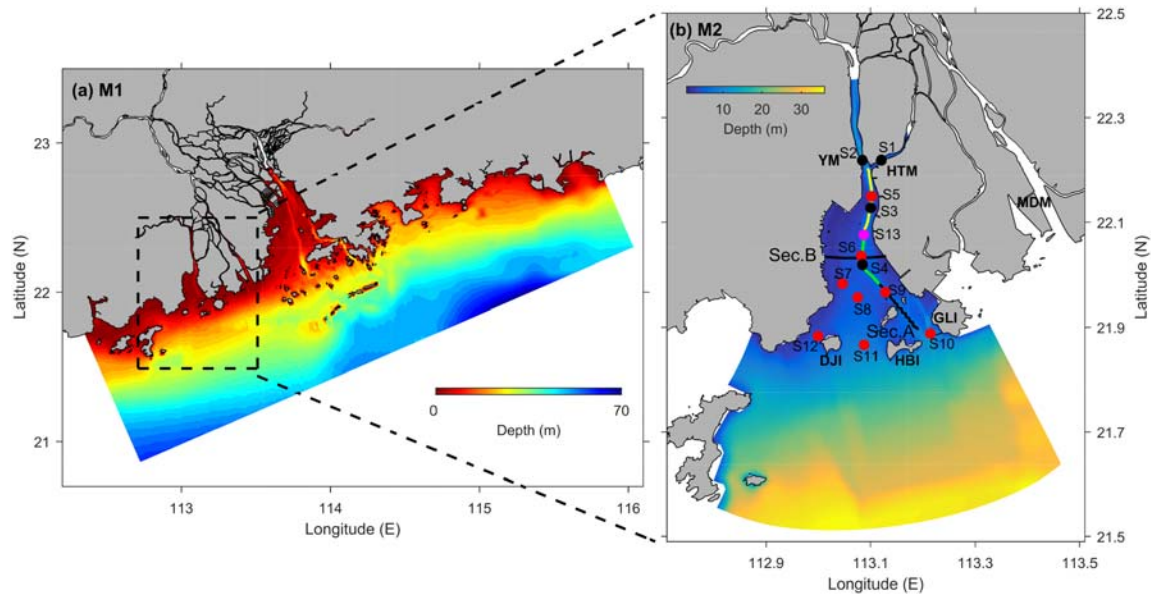
Figure 1. Major topographic features and domains of the nested modeling system over (a) the Pearl River Delta and (b) the HE and its adjacent waters. YM = Yamen; HTM = Hutiaomen; MDM = Modaomen; DJI = Dajing Island; GLI = Gaolan Island; HBI = Hebao Island. The black dots (S1–S4) and red dots (S5–S12) in M2 are stations for field deployments in June 2010 and July 2012, respectively. The solid lines represent the along-channel and cross-channel transects, which are Sec. A and Sec. B, respectively. Sec. A consists of three sections: the upper bay (yellow line), the middle bay (blue line), and the lower bay (black line). The magenta dot in Sec. A (S13) is for sediment flux decomposition in section 5.2.2.

effects of wind waves on currents and sediment transport as waves are generally weak during wet seasons (from May to October) in the HE (Gong et al., 2014). The HE has predominantly mixed semidiurnal tides, and the annual averaged tidal ranges at Hebao Island and YM are 1.34 and 1.25 m, respectively, indicating a microtidal regime. The bathymetry of the bay is complicated, exhibiting three shoals (mouth sandbar shoal, western shoal, and eastern shoal) and three channels (ebb main channel at the head of the estuary, east navigation channel, and west navigation channel) (Gong et al., 2014).

The river discharge and riverine sediment delivered to the estuary comes primarily from the YM (downstream of the Tanjiang River) and HTM outlets. The annual average river discharge and riverine sediment from the YM outlet are 19.6×10^8 m^3 (49.2% of the total river discharge) and 3.63×10^6 t, respectively, whereas those from the HTM outlet are 20.2×10^8 m^3 and 4.99×10^6 t, respectively. Affected by the monsoon climate, the river runoff features a pronounced seasonal variation, and 80% of the discharge occurs in the wet season, with an averaged river discharge of 200.23 m^3 s^{-1} during the wet season and 61.01 m^3 s^{-1} during the dry season (from December to February). The strength of the vertical stratification in the HE is primarily controlled by the seasonal change in river runoff and spring-neap variation in tidal mixing, resulting in partially mixed to highly stratified conditions during the wet season and well-mixed to partially mixed conditions during the dry season (Gong et al., 2014). In this paper, we focus on the wet season, when the HE typically exhibits partially mixed conditions during the spring tide and highly stratified conditions during the neap tide.

Due to the subtropical monsoon climate, winds in the HE exhibit significant seasonal variation, with northeasterly (down-estuary) winds during the dry season and southwesterly (up-estuary) winds during the wet season. The mean wind speeds during the dry season and the wet season are 6.7 and 4.5 m s^{-1}, respectively.

The riverine sediment is composed of fine particles (silt or clay), whereas the bottom sediment at the estuary mouth mainly consists of medium-grained sand. At the HE bay, the main component of the bottom sediment is silty clay or silt (<0.008 mm) at the western shoal and eastern shoal and other shallow regions, whereas fine- or medium-grained sands are dominant in the ebb main channel and navigation channels. Due to frequent dredging, the bottom sediment composition in the channels changes frequently and contains some coarser-grained sands.

3. Methodology

The observations conducted in the HE is generally short termed and of low spatial resolution, which is not sufficient for studying the dynamics controlling sediment transport in the estuary. To complement this shortcoming, a nested ocean modeling system was developed (Figure 1). The model system consists of two nested grids to enable finer horizontal resolution from the PRD to the HE.

3.1. Numerical Model Setting

The parent model, based on a 1-D (for the river network, called Riv1D) and 3-D (for the Pearl River Estuary, PRE) coupled model, covered the whole PRD and the coastal region, including Hong Kong, with a horizontal resolution of 2 km near the open boundary and 500 m inside the PRE (Figure 1a). The 3-D hydrodynamic model used was a free-surface, primitive-equation ocean model called the Estuarine, Coastal and Ocean Model (Blumberg, 2002). There were a total of 363×196 grid cells in orthogonal curvilinear coordinates and 16 equally spaced σ levels in the vertical. The seaward boundary of the parent model was parallel to the Guangdong coast and roughly followed the 70 m isobath. The topography for the parent model was derived from the bathymetry of the General Bathymetric Chart of the Oceans 1 arcmin global bathymetric data set. For detailed description of the 1D and 3D coupled model, see Hu et al. (2011).

The inner-child model, based on the COAWST system, covered the entire HE and part of the continental shelf in the northern South China Sea, and it had high resolution in both the horizontal and vertical directions (Figure 1b). An orthogonal curvilinear coordinate system was applied, with a grid spacing less than 1.5 km near the open boundary and a refined horizontal resolution of 50 m in the channel and up-estuary river network. The model domain contains 235×243 horizontal grid cells and 21 vertical terrain-following s-levels. The bathymetry data for the child model were digitized from the navigational chart released by the Maritime Safety Administration of the People's Republic of China.

3.2. Model Forcing

For the Riv1D parent model, daily Pearl River discharge data were provided by the Pearl River Water Resources Commission of the Ministry of Water Resources. The 3-D parent model was driven by atmospheric forcing and lateral open-boundary conditions. The atmospheric forcing consisted of 6-hourly wind stress estimates from the Climate Forecast System Reanalysis model (CFSR; Saha et al., 2010), with a horizontal resolution of 0.3°. The lateral open-boundary conditions for the parent model comprised (1) hourly tidal elevations and depth-averaged tidal currents derived from nine tidal constituents (M_2, S_2, N_2, K_2, K_1, O_1, P_1, Q_1, and M_4) taken from the global tidal circulation model (TPXO 8, http://volkov.oce.orst.edu/tides/tpxo8_atlas.html) with a resolution of 1/30° and (2) daily water elevation, 3-D temperature, salinity, and velocity data from the Hybrid Coordinate Ocean Model (https://hycom.org) with a resolution of 1/12°. The lateral open-boundary condition for the child model was based on the conventional one-way nesting technique.

The child model was initialized with the outputs of salinity and temperature from the parent model, and the water elevation, velocity, and sediment concentration in the interior domain were initialized as zero. Along the open boundaries, the implicit gravity wave radiation boundary condition (Chapman, 1985) was used for the sea surface elevation, whereas the radiation open-boundary condition suggested by Flather and Davies (1976) was used for the depth-averaged barotropic velocity. Radiation and nudging boundary conditions were adopted for the temperature, salinity, and sediment. The vertical mixing coefficient in the child model was calculated using the $k - \varepsilon$ module of the generic length-scale method (Umlauf & Burchard, 2003).

3.3. Sediment Modeling

We used the Community Sediment Transport Model (Warner et al., 2008) to simulate sediment transport. Suspended sediment was introduced into the model through river runoff at river discharge points, at open ocean boundaries, and from seabed erosion. Five sediment classes were used, and their relevant parameters are listed in Table 1. There were two fluvial sediment classes and three estuarine sediment classes, each with a unique sediment grain size. The critical shear stresses for erosion were determined based on the Shields curve, with slight adjustment made to minimize the model-data misfit (Cheng et al., 2013; Gelfenbaum & Smith, 1986). The background vertical diffusion coefficients of 5×10^{-6} m^2 s^{-1} and sediment density of 2,650 kg m^{-3} were chosen for all sediment classes. The critical shear stress for deposition was set to

Table 1
Parameters for the Community Sediment Transport Model (CSTM)

Sediment parameters	Fluvial sediment		Bay bottom sediment		
	Clay1	Silt1	Clay	Silt	Fine sand
Grain size (mm)	0.003	0.015	0.006	0.030	0.125
Settling velocity (mm s^{-1})	0.08	0.2	0.08	0.35	1.0
Critical shear stress (Pa)	0.05	0.05	0.1	0.12	0.4
Erosion constant (kg m^{-2} s^{-1})	1×10^{-3}	1×10^{-4}	1×10^{-4}	1×10^{-4}	1×10^{-5}
Fraction (%)[a]	60	40	−	−	−
Bottom porosity	0.7	0.7	0.7	0.7	0.7

[a]The fraction of bay bottom sediment is spatially varying.

2.0 N m^{-2} to ensure that all suspended sediments settle down when reaching the bed. The sediment particles' settling velocities (w_s) were determined based on experimental data (Xia et al., 2004). We also adjust the settling velocities to minimize the model-data misfit (Table 1). The chosen settling velocities are within the range reported in a numerical study in the PRE (Zhang et al., 2019). The initial sediment bed was set with two layers with 0.02 m in the upper layer and 3.0 m in the bottom layer. The total initial sediment thickness of 3.02 m ensured sufficient sediment supply for subsequent erosion. In this study, the contribution of suspended sediment to water density was not considered as the suspended sediment concentration (SSC) was generally less than 0.4 g L^{-1} in our study site. The cohesive sediment consolidation, aggregation, and disaggregation processes were simply neglected.

In this study, the initial distribution of the three estuarine sediment classes was obtained from surficial sediment samples, which were collected in the HE at 104 site in 2011 (Jia & Yi, 2013) and 63 sites in 2018 (Figure 2a). We obtained the spatial distribution of fractions of these sediment classes by utilizing a combination of interpolation and extrapolation owing to the insufficient sediment samples. Both the surface sediment concentration derived from the Moderate Resolution Imaging Spectroradiometry (MODIS) and the observed SSC around the chain of rocky islands (S10–S12 in Figure 1a) are relatively low, indicating that local sediment resuspension is weak and the extrapolation results might underestimate the fraction of coarser-grained sands there. Thus, in regions lacking direct observations of surficial sediment grain size, such as south of the chain of rocky islands, the sediment was simply considered as sand because the grain size around the estuary mouth is generally coarser than those inside the estuary. Note that there may be differences between grain sizes obtained from surficial samples in 2011 and 2018. Hence, it may not be appropriate to initiate sediment simulation only by utilizing the observed sediment composition derived from surficial sediment samples. Inspired by the optimization procedure suggested by Sassi et al. (2015), the model was run from 16 April to 1 July 2010, and then it was reinitialized with outputs at the end of simulation. This procedure was repeated three times, and the sediment concentration in the HE reached a quasi-static cyclic variation between spring and neap tides. The resulting sediment distribution at the end of the last iteration was utilized to initialize the sediment module, shown in Figures 2b–2d. Although some studies recommend yearly spin-ups to initialize the sediment bed (Grasso et al., 2018; Van Der Wegen et al., 2011), we found that three iterations of cyclic run can resolve the sediment distribution well and save computational cost. The details of model validation are presented in Appendix A.

4. Results

The time series of wind, water elevation, and river discharge for the period from 16 April to 1 July 2010 (76 days) are shown in Figure 3. The wind speed varied from 4 to 10 m s^{-1}, and the wind direction changed at synoptic time scales. The winds were predominately southerly, with intermittent winds from NE and north (Figure 3a). Neap and spring tides alternately influenced the water elevation at the estuary mouth (Figure 3b). The river discharge was low during the first half of the simulation period but increased by nearly 15 times during the rest of the period, with a minimum discharge from the Pearl River of 1,400 m^3 s^{-1} on 16 April (Day 1) and a maximum discharge of 26,400 m^3 s^{-1} on Day 63 (Figure 3c).
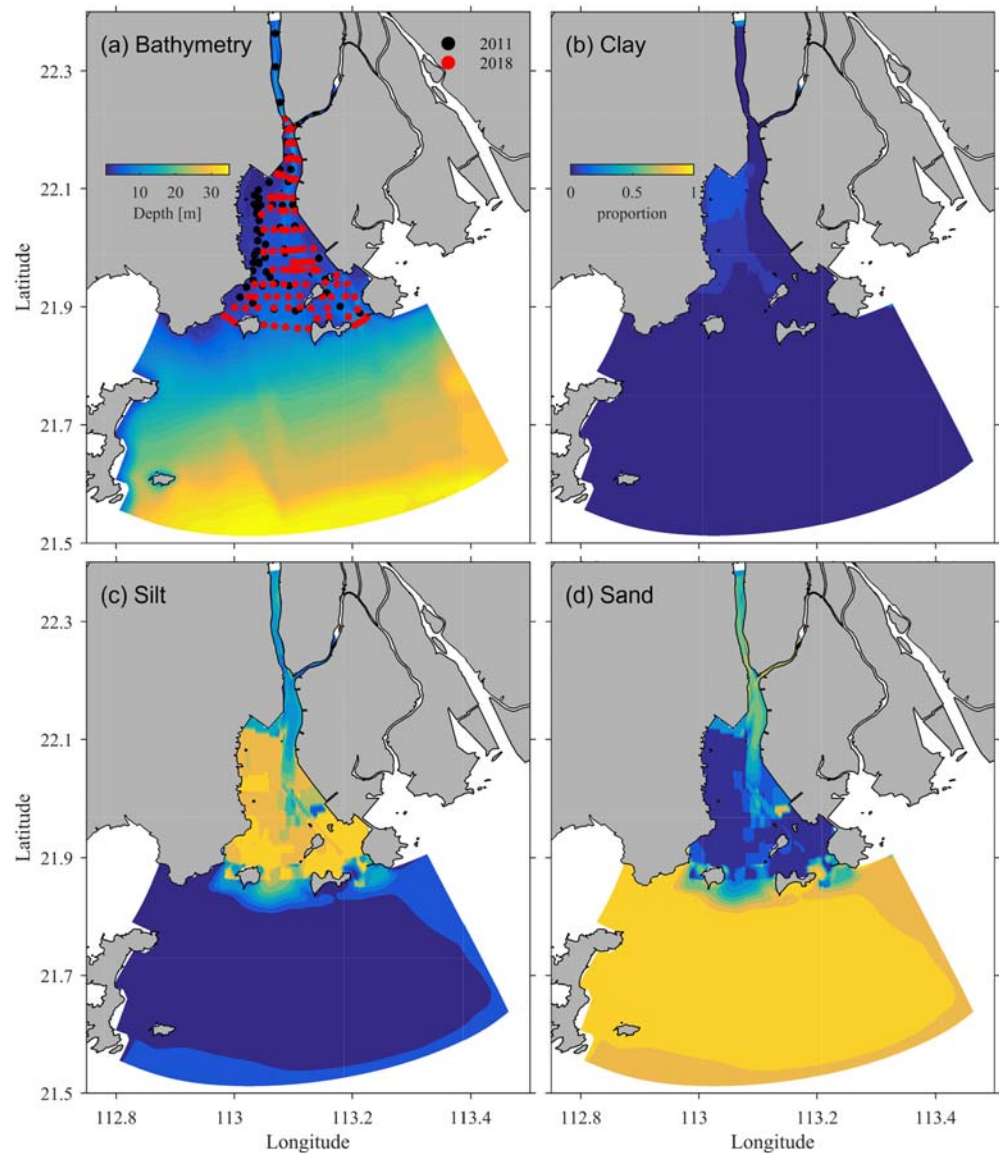
Figure 2. (a) Bathymetry in the HE and sediment sample stations, including 104 sites in 2011 and 63 sites in 2018. The sediment fraction distribution of (b) clay, (c) silt, and (d) sand in the HE.

Winds in the estuary were always southerly (up-estuary) from Days 58 to 76, so this period was utilized to examine up-estuary wind effects in the HE. To distinguish the effects of wind forcing, we ran two additional model simulations, one without wind forcing and the other with down-estuary winds, in which the wind speeds from Days 58 to 76 were kept unchanged, while the wind directions were reversed, i.e., changing the up-estuary winds to down-estuary winds.

4.1. Response of Longitudinal Dynamics to Down- and Up-Estuary Winds

A comparison of subtidal salinity, current, SSC, and eddy diffusivity along a chosen longitudinal section (Sec. A in Figure 1b) at the neap tide (Day 66) for down-estuary wind, no-wind, and up-estuary wind model runs is shown in Figure 4. A 34-hr low-pass filter was applied to remove tidal oscillations. Without wind forcing, the estuary exhibited two-layer gravitational circulation, with seaward subtidal flow at the surface and landward residual flow at the bottom. The maximum residual flow was on the order of 0.6 m s^{-1}, appearing in the upper bay, and the exchange flow in the HE decreased gradually from the upper bay to the lower bay (Figure 4g). The lateral flow showed a pattern with eastward flow at the surface and westward flow at the
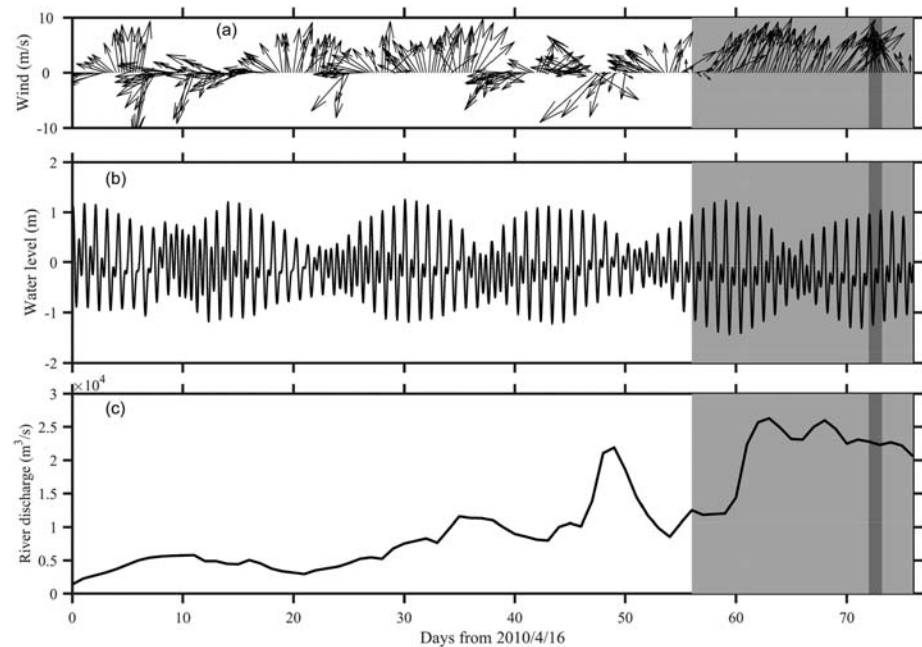
Figure 3. The external forcings during the model simulation period from 26 April 2010. (a) Time series of wind at the YM derived from CFSR reanalysis data set; (b) water elevation at the estuary mouth; (c) daily river discharge (the total discharge from the West, North and East Rivers). The study period for investigating wind effects is shaded in gray, and the period of observation deployment is shaded in dark gray.

bottom in the lower bay and upper bay and a reversed pattern in between (Figure 4h). Strong stratification was observed in the middle bay, with surface-to-bottom salinity differences reaching 10–12 psu (Figure 4f). Owing to the strong currents in the upper bay and abundant fluvial sediment input by river inflow, high SSC water appeared in the upper bay, with a peak subtidal SSC of 0.46 g L^{-1} at the bottom (Figure 4i), where the subtidal surface-to-bottom current difference reached 0.7 m s^{-1}. Longitudinal convergence of suspended sediment transport resulted in a clear estuarine turbidity maximum in the upper bay. Strong turbulent mixing due to tidal currents resulted in high values of eddy diffusivity (~10^{-6} m^2 s^{-1}) in the middle around 2–4 m (Figure 4j). Because abundant fresh water brought by river inflow reduced the salinity stratification, vertical mixing in the upper bay was relatively strong (~10^{-5} m^2 s^{-1}).

Up-estuary winds drove a landward-directed current in the surface and seaward current at the bottom, opposing the gravitational circulation in the HE. As a result, the exchange flow was decreased by 52.2%, with peak seaward current at the surface reduced from 0.67 to 0.32 m s^{-1} (Figure 4l). Up-estuary winds also drove Ekman lateral flows in the lower bay, increasing the eastward current at the surface from 0.18 to 0.37 m s^{-1} and doubling the westward current at the bottom (Figure 4m). Influenced by the weakened exchange flow, the longitudinal salinity structure was different from the model run without wind. The water column was more mixed in the upper bay but more stratified in the lower bay under up-estuary winds (Figure 4k). The wind-driven mixing steepened the isopycnals in the surface layer (<2 m) in the middle and lower bays.

During up-estuary winds, there was a 32% reduction in the subtidal SSC at the bottom in the upper bay. The location of the estuarine turbidity maximum, with a maximum SSC of 0.28 g L^{-1}, moved from the upper bay to the upper-middle bay junction (~10 km), where the subtidal flow at the bottom was almost zero (Figure 4n). Meanwhile, SSC in the surface layer in the upper bay increased notably owing to the enhanced vertical mixing, decreasing the vertical gradient of SSC. There were several notable changes in the eddy diffusivity (Figure 4o). First, its magnitude in the middle and lower bays increased slightly (~10^{-8} m^2 s^{-1}) in the surface layer (<2 m) owing to the wind-driven mixing but decreased significantly from 10^{-6} to 10^{-7} m^2 s^{-1} in the middle layer. Moreover, there was a notable increase in eddy diffusivity (>10^{-4} m^2 s^{-1}) in the upper bay where well-mixed conditions prevailed. The mechanism driving this change is discussed in section 5.1.
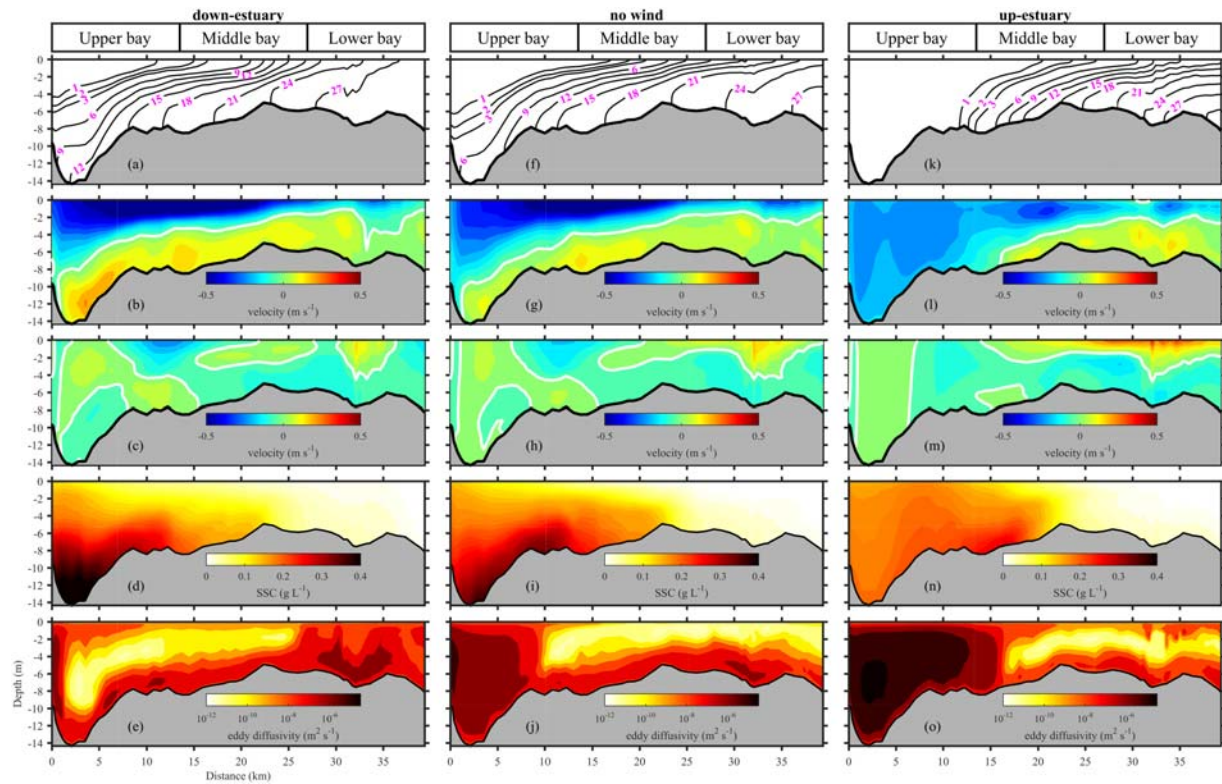
Figure 4. Along-channel distributions of (a, f, k) subtidal salinity, (b, g, i) axial current, (c, h, m) lateral flow, (d, i, n) SSC, and (e, j, o) the eddy diffusivity at Sec. A on Day 57 (neap tide) when up-estuary wind prevails. The zero axial current is marked as a white solid line. The positive for axial flows means landward.

Under the down-estuary winds, the longitudinal distributions of the axial current, salinity, and SSC were very similar to those of the model run without wind (Figures 4a, 4b, and 4d). The wind-driven two-layer circulation slightly amplified the two-layer gravitational circulation (Table 2). The wind-driven lateral flow reduced the eastward current at the surface by one half (Figure 4c). The surface-to-bottom salinity difference increased from 8 to 11 psu in the upper bay but decreased from 8 to 4 psu in the lower bay. Thus, down-estuary winds increased stratification in the upper bay and reduced stratification in the lower bay (Figure 4a). This pattern is opposite to the changes in vertical stratification under up-estuary winds and is discussed in section 5.1. The magnitude of subtidal SSC increased by 21.6% under down-estuary winds, indicating that down-estuary winds generated sediment entrapment in the upper bay (Figure 4d). The significant decrease in vertical stratification in the lower bay allowed elevated eddy diffusivity to extend throughout much of the water column (Figure 4e).

During spring tides, there was a significant reduction in the estuarine exchange flow. Because tidal mixing was dominant during these periods, axial winds played a similar but weakened role to that during the neap tide in modulating exchange flow, lateral circulation, and the corresponding increase/decrease in stratification and SSC (Table 2). Thus, we do not present the details of axial winds effects during spring tides; instead, we present the subtidal peak values in Table 2.

4.2. Response of Lateral Dynamics to Down- and Up-Estuary Winds

The lateral distributions of salinity, axial current, lateral current, along-channel vorticity ($\omega = \frac{\partial w}{\partial x} - \frac{\partial u}{\partial z}$), and SSC at a cross section (Sec. B in Figure 1a, looking landward) in the middle bay during the neap tide are shown in Figure 5. Without wind forcing, the outflow was concentrated near the surface over the channel and the western shoal, whereas inflow was mainly in the bottom layer over the eastern shoal (Figure 5f). Anticlockwise circulation occurred over the western shoal, whereas strong clockwise circulation was present over the eastern side of the channel (Figure 5g). The main characteristics of the lateral flow are consistent with previous observations in the Chesapeake Bay (Li & Li, 2011) and in the analytical model results of

Table 2
Subtidal Peak Value of Gravitation Circulation ($m\ s^{-1}$) and SSC ($g\ L^{-1}$) for Numerical Simulations Without Wind and Under Down- and Up-Estuary Winds

Subtidal peak value		Down-estuary wind	No wind	Up-estuary wind
Neap	landward current	0.15	0.12	0.12
	Seaward current	0.60	0.58	0.38
	SSC	0.22	0.25	0.20
Spring	landward current	0.08	0.09	0.08
	Seaward current	0.44	0.40	0.34
	SSC	0.48	0.42	0.35

Huijts et al. (2009). At the subtidal time scale, the isopycnals generally sloped downward toward the west, consistent with the thermal wind relationship (Figure 5e). SSC was elevated near the bed over the western shoal, consistent with a convergence in lateral flux at this location (Figure 5h).

For the model run with up-estuary winds, the exchange flow was weakened; this weakening was observed as a decrease in both the outflowing and inflowing velocities. Influenced by the wind-driven lateral flow, the associated anticlockwise circulation over the western shoal disappeared, and the clockwise circulation over the eastern shoal were enhanced to occupy the whole cross section (Figure 5k). The position of peak outflow also shifted eastward from the channel to the eastern shoal, and the low-salinity water was advected from the western shoal to the surface of the channel, significantly reducing the lateral salinity gradient (Figure 5i). The SSC at the western shoal was reduced by nearly 30% (Figure 5l). The mechanism for such a change is discussed in section 5.2.

Under down-estuary winds, both outflow and inflow increased slightly, resulting in an enhanced exchange flow (Figure 5b). Wind-driven surface Ekman transport, which was directed westward, enhanced the corresponding anticlockwise circulation over the western shoal but slightly reduced the clockwise circulation over the eastern shoal (Figure 5c). Influenced by the lateral flow structure, high-salinity water was transported from the eastern side of the channel to the western shoal, steepening the isohalines in the upper 3 m and slightly increasing the lateral salinity gradient (Figure 5a). Consistent with both the up-estuary and no-wind model runs, SSC was elevated over the western shoal (Figure 5d). The distribution of tidally averaged sediment did not change notably with the down-estuary winds. Further analysis about the SSC change is presented in section 5.2.

4.3. Axial Wind Effects on Stratification

As shown in Figure 4, estuarine stratification was strongly influenced by the axial winds and exhibited a remarkable asymmetric response to wind directions in different locations: The stratification increased in the upper bay but decreased obviously in the lower bay under the down-estuary winds, and the opposite occurred under the up-estuary winds. To quantify the stratification change, we calculated the volume-averaged buoyancy frequency (N^2) under different winds by averaging over the upper bay section and the lower bay section along Sec. A. Because our observation showed that stratification in the estuary was mainly controlled by the salinity difference, the equation for calculating the buoyancy frequency neglected the contribution of temperature on density by adopting $N^2 = -g\beta\frac{\partial S}{\partial z}$. β is the saline contraction coefficient (7.7×10^{-4}), as proposed by Xie and Li (2018).

Without wind forcing, N^2 fluctuated substantially over a tidal cycle during spring tides: N^2 increased gradually during early ebb and peaked at maximum ebb, and then it decreased significantly during flood tides (Figure 6). N^2 showed obvious spring-neap variation owing to a change in tidal mixing, with larger magnitude during neap tides than during spring tides.

As shown in Figure 6a, N^2 increased slightly under down-estuary winds but decreased significantly under up-estuary winds in the upper bay. Under up-estuary winds, the maximum N^2 reduction occurred during the neap tide, and the averaged N^2 decreased almost to zero. Stratification changes in the lower bay showed an opposite pattern: The volume-averaged N^2 decreased by one half under down-estuary winds but doubled under up-estuary winds during the neap tide (Figure 6b). Compared to the N^2 changes during the neap tide, changes in stratification were less significant during spring tides. The opposite response of the upper and
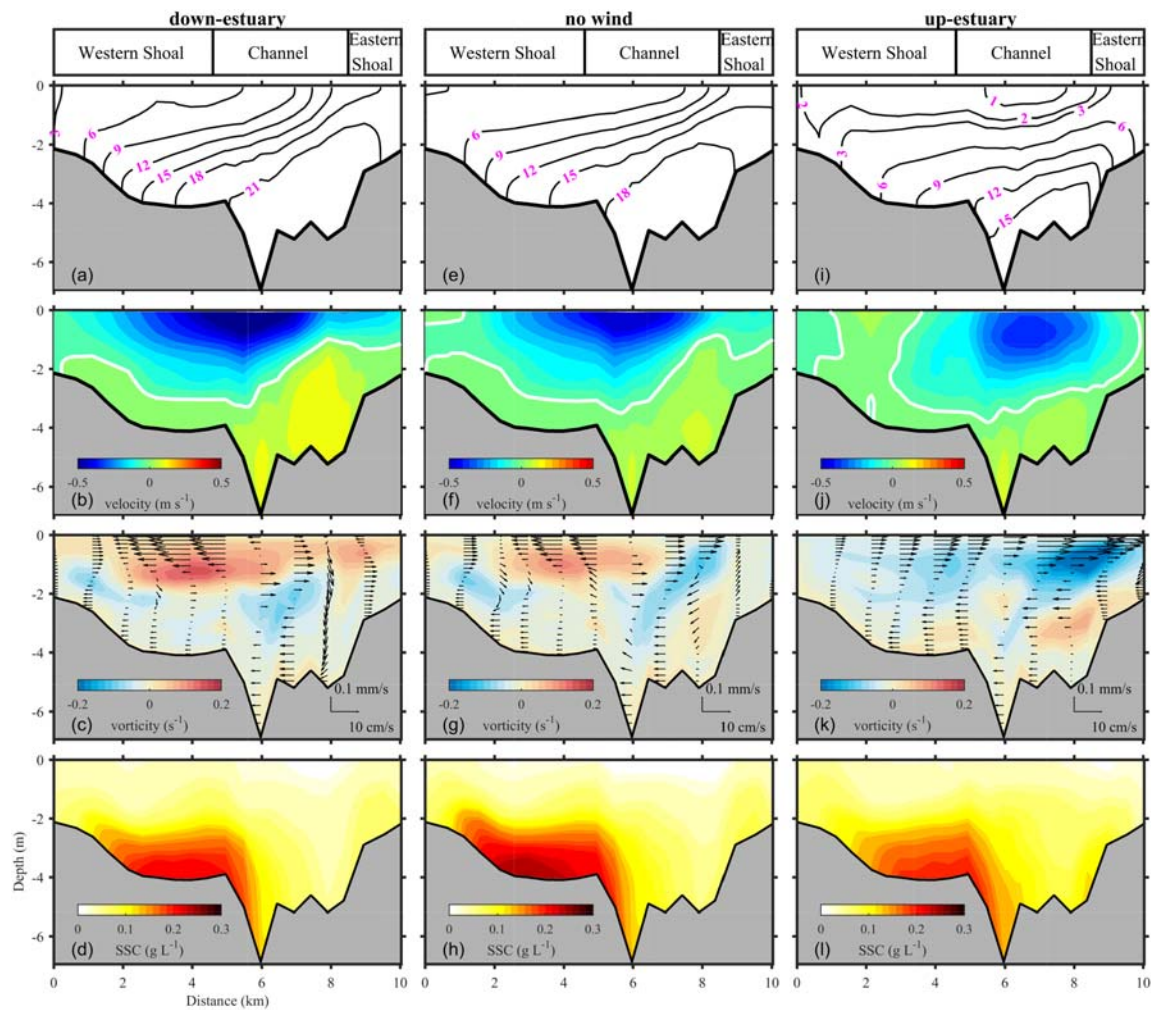
Figure 5. Cross-channel distributions of (a, e, i) subtidal salinity, (b, f, j) axial current, (c, g, k) cross-channel vorticity (contours) and lateral current (arrows), and (d, h, l) the SSC at Sec. B on Day 57 (neap tide) when up-estuary wind prevails. The zero axial current is marked as a white solid line. The view of Sec. B is looking landward, and the positive for axial flows means landward.

lower bay regions to axial winds is not consistent with the effects of longitudinal wind straining (Scully et al., 2005), and lateral wind straining (Li & Li, 2011) and wind-driven mixing (Chen & Sanford, 2009a), but this pattern may be induced by the combined contributions of along-channel wind straining and cross-channel wind straining, as proposed by Xie and Li (2018). The associated mechanism is discussed in section 5.1.

4.4. Axial Wind Effects on Suspended Sediment Flux

During the neap tide (Day 66), the residual suspended sediment flux was generally smaller than 1.5×10^4 kg m^{-1} inside the HE bay, with higher sediment flux located in the HTM and YM outlets associated with an abundant source of riverine sediment (Figure 7). Under the up-estuary winds, the down-estuary sediment flux in the northern part of the ebb main channel increased by nearly 10 times, reaching a magnitude of 3.8×10^4 kg m^{-1} (Figure 7f). The up-estuary winds also altered the lateral flow structure and changed the direction of sediment flux in the middle and lower bays (Figure 7f). Under the down-estuary winds, the sediment flux did not change notably. In general, the up-estuary winds tended to advect suspended sediment seaward, whereas the down-estuary winds favored sediment trapping in the upper bay or at the head of the estuary (Figure 7b). During spring tides, the suspended sediment flux was large (nearly 6.1×10^4 kg m^{-1}) at the YM and HTM outlets and tended to be strongest in the northern part of the ebb main channel owing to enhanced resuspension (7.2×10^4 kg m^{-1}) (Figure 7c). Due to the
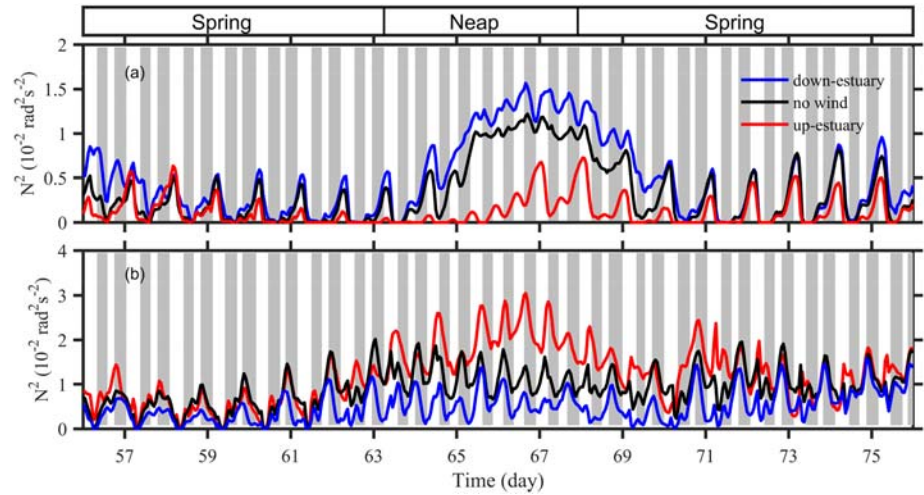
Figure 6. Time series of volume-averaged buoyancy frequency for model runs under down-estuary wind (blue), up-estuary wind (red), and without wind forcing (black) at (a) the upper bay section and (b) the lower bay section along Sec. A. The flood phases are shaded in gray.

strong river discharge, sediment flux was mainly seaward in the channels and over the eastern shoal (Figure 7c). The result demonstrated that westward flow advected suspended sediment to the western shoal, resulting in sediment entrapment there (Figure 7c). When axial winds were applied, the seaward sediment flux in the upper bay increased by 19.2% under the up-estuary winds (Figure 7e) but decreased by nearly 30% under the down-estuary winds (Figure 7a). The sediment flux in the lower bay increased slightly under the axial winds owing to wind-driven lateral circulation. During spring tides, the axial winds altered the direction of sediment transport, especially on the western shoal, but this effect was less remarkable than that during the neap tide.

As shown above, the wind events had great impact on the hydrodynamics and sediment transport in the estuary, the question as to how often these wind events occur arises. The wind data during wet seasons from 1992 to 2017 (26 years) were collected from the CFSR data because there is no long-term wind measurements in the HE. The high-frequency fluctuations in the time series of wind speed was removed by a 34-hr low-pass filter. Weak winds were ignored when the wind speed was less than 4 m s^{-1}, as suggested by Xie and Li (2018). It showed that wind events with a wind speed of >4 m s^{-1} occurred in more than 60% of the investigated period in the HE, with up-estuary wind events accounting for 42.4% and down-estuary wind events accounting for nearly 19.8%. This indicated that wind events are quite often in the HE and are an important component of forcings that govern the hydrodynamics and sediment dynamics in the estuary.

5. Discussion

5.1. Lateral Versus Longitudinal Wind Straining on Stratification in the HE

To illustrate how the down-estuary and up-estuary winds influence the stratification in the HE, we quantified the different terms in the stratification equation. The buoyancy frequency over time can be decomposed into three components:

$$\frac{\partial N^2}{\partial t} = \underbrace{-\left(u\frac{\partial N^2}{\partial x} + v\frac{\partial N^2}{\partial y} + w\frac{\partial N^2}{\partial z} \right)}_{\text{advection}}, \tag{1}$$

$$\underbrace{+ g\beta\frac{\partial S}{\partial x}\frac{\partial u}{\partial z} + g\beta\frac{\partial S}{\partial y}\frac{\partial v}{\partial z} + g\beta\frac{\partial S}{\partial z}\frac{\partial w}{\partial z}}_{\text{straining}},$$
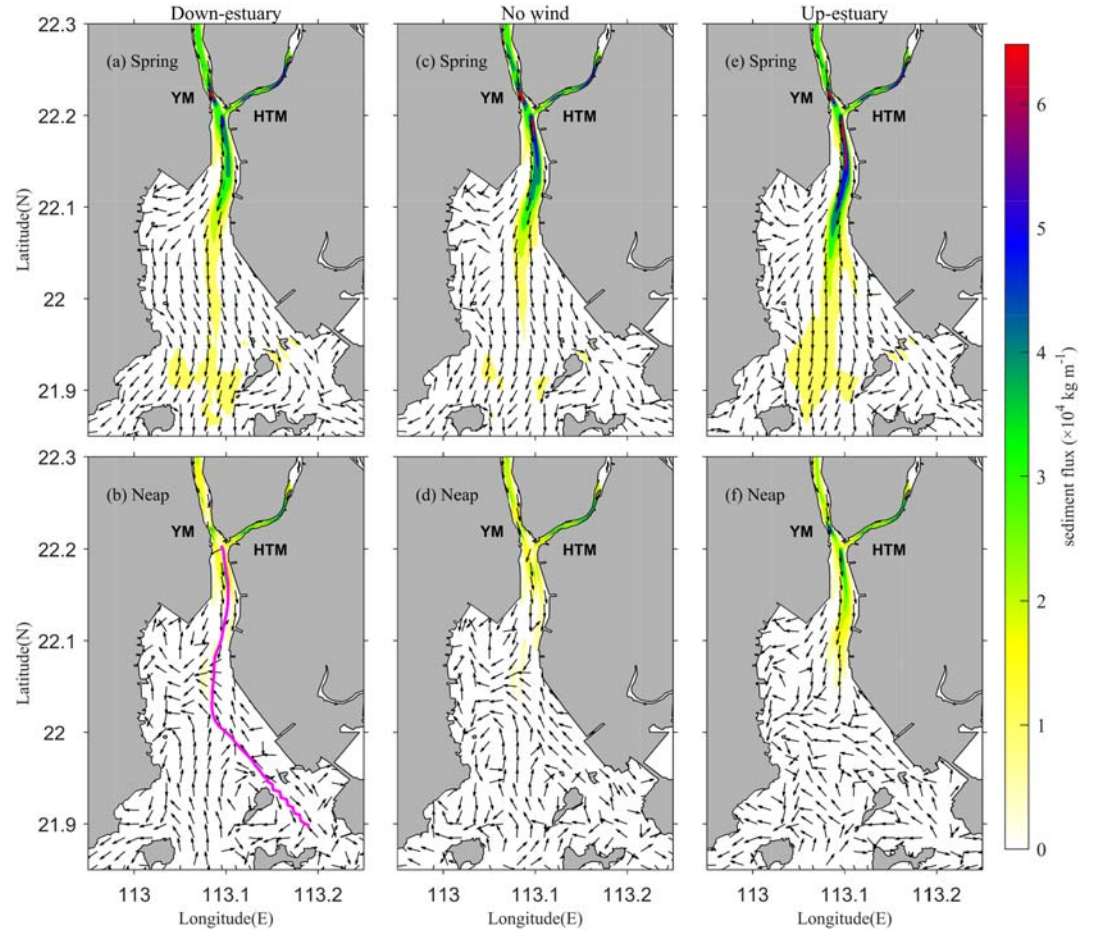
Figure 7. The suspended sediment flux integrated vertically and in tidal time scale (kg m^{-1}) (a, b) under down-estuary wind, (c, d) without wind forcing, and (e, f) under up-estuary winds. The (top) spring (Day 53) and (bottom) neap tides (Day 58). For viewing purposes, the arrows have an identical length and only represent the direction of suspended sediment flux. The magenta line in (b) represents the thalweg in the HE bay.

$$-g\beta\underbrace{\left[\frac{\partial^2}{\partial z^2}\left(K_S\frac{\partial S}{\partial z}\right)+\frac{\partial^2}{\partial z\partial x}\left(K_H\frac{\partial S}{\partial x}\right)+\frac{\partial^2}{\partial z\partial y}\left(K_H\frac{\partial S}{\partial y}\right)\right]}_{\text{diffusion}},$$

where S is the salinity; u, v, and w are the velocity components in the cross-channel (x), along-channel (y), and vertical (z) directions, respectively; K_S and K_H are the vertical and horizontal eddy diffusivities, respectively; and g is the gravitational acceleration. At each model grid point, the velocity was decomposed into the along-channel (x) and cross-channel (y) components (u, v), as proposed by Li and Li (2012). We chose the major axis of the depth-averaged current as the along-channel direction (positive northward), while the cross-channel direction was defined to be perpendicular to the along-channel direction (positive eastward), as proposed by Xie and Li (2018). The first three terms on the right-hand side of equation (3) are the advective terms, the next three terms represent straining, and the last three terms are turbulent diffusion. More details about the stratification equation are in Li and Li (2011). In this study, we integrated the equation over a control volume to evaluate the overall balance in the stratification equation by adopting the method proposed by Li and Li (2012), defined as

$$\overline{N}^2=\frac{\int_A\left[\overline{N}^2\right]_z dA}{\int_A dA},\qquad(2)$$

where $\left[\overline{N^2}\right]_z = \dfrac{\int_{-h}^{\zeta} N^2 dz}{\int_{-h}^{\zeta} dz}$ and A is the area of the selected region. We selected two control volumes: one is the upper bay section along Sec. A (yellow line in Figure 1b) and the other is the northern half of the lower bay section along Sec. A (black line in Figure 1b). At the southern half of the lower bay section, the surrounding rocky islands may influence the water current and salinity structure, which makes it difficult to distinguish the mechanism. Hence, only the northern half of the lower bay section was selected as the control volume.

5.1.1. Stratification Dynamics in the Lower Bay

First, we examined all the terms in the stratification equation in the lower bay by integrating the volume averaged terms in time (from Day 57, $\left.\left|\overline{N^2}\right|\right|_t = \int_{t_0=57}^{t} \overline{N^2} dt$); thus, the overall effect of axial winds on stratification can be evaluated. Without wind forcing, the integration of turbulent diffusion decreased at a fixed rate (Figure 8c). A quasi-steady condition was achieved by the straining (positive) balancing the turbulent diffusion (negative). The integration of the advective terms was relatively small (<-0.10 s^{-2}), indicating that advection contributed little to the variation of stratification in an integrated sense.

Including axial wind forcing resulted in large differences in the total contribution of the straining terms between the up-estuary and down-estuary winds. The integration of the straining term on Day 76 decreased to 0.36 s^{-2} during the down-estuary winds (Figure 8a) but increased to 1.16 s^{-2} (3.2 times larger) under the up-estuary winds (Figure 8e). To better understand these differences, we decomposed the straining terms into the u, v, and w directions. Without wind forcing, all three straining terms were positive, with magnitudes ranging from 0.23 to 0.40 s^{-2} (Figure 8d). Under the up-estuary winds, the lateral straining term ($\frac{\partial S}{\partial x}\frac{\partial u}{\partial z}$) doubled and the other two straining terms decreased slightly (Figure 8f). With the down-estuary winds, the integration of $\frac{\partial S}{\partial x}\frac{\partial u}{\partial z}$ decreased to almost zero and had the opposite sign (-4.4 psu m^{-1}) to that with the up-estuary winds (Figure 8b). Meanwhile, the integrations of $\frac{\partial S}{\partial y}\frac{\partial v}{\partial z}$ and $\frac{\partial S}{\partial z}\frac{\partial w}{\partial z}$ decreased by 43% and 45%, respectively. The results demonstrated that the stratification change in the lower bay was strongly influenced by the cross-channel wind straining term. Under the up-estuary winds, a clockwise lateral Ekman circulation developed in the lower bay and advected the low-salinity water from the west shoal to the main channel near the surface. Meanwhile, the saltier water in the bottom layer flowed toward the west, generating a remarkable lateral tilt of the isopycnals and inducing weak lateral density gradient but obvious vertical stratification (Figures 5i and 5k). For the down-estuary winds, wind-driven lateral flow with distinct vertical shear acted on the salinity field to lift isopycnals and thus decreased estuarine stratification (Figures 5a and 5c).

5.1.2. Stratification Dynamics in the Upper Bay

Next, we investigated the situation in the upper bay. The vertical stratification in the upper bay depended on the balance between the turbulent mixing (negative) and the straining (positive) (Figure 9c), similar to that in the lower bay. In response to the down-estuary winds, the integrated straining terms increased significantly, with a peak value of 0.59 s^{-2} (Figure 9a). In contrast, the up-estuary winds decreased the total straining by one half, reaching a maximum of 0.23 s^{-2} on Day 76 (Figure 9e). Similar to the situation in the lower bay, asymmetries in the straining terms played a dominant role on the stratification changes in response to axial winds. As shown in Figure 10d, the integrated straining terms during the neap tide were much larger than those during the spring tide. Compared to that in the lower bay, the lateral straining term changed little (less than 0.10 s^{-2}) under different wind conditions (Figures 9b and 9f). However, unlike that in the lower bay, longitudinal straining was much larger, reaching a maximum of 0.43 s^{-2} on Day 76 without wind forcing (Figure 9d). Longitudinal straining also responded asymmetrically, with peak values reaching 0.08 s^{-2} under the up-estuary winds (Figure 9f) and 0.62 s^{-2} (7.8 times larger) under the down-estuary winds (Figure 9b). Hence, the along-channel wind straining played a dominant role in driving stratification changes in the upper bay.

5.2. Influences of Axial Wind on Longitudinal Sediment Flux

In the following section, we assessed the axial wind effects on sediment transport and analyzed how the longitudinal SSC flux responded to the estuarine stratification changes analyzed above. We also investigated the interaction between stratification and longitudinal SSC flux in the HE.
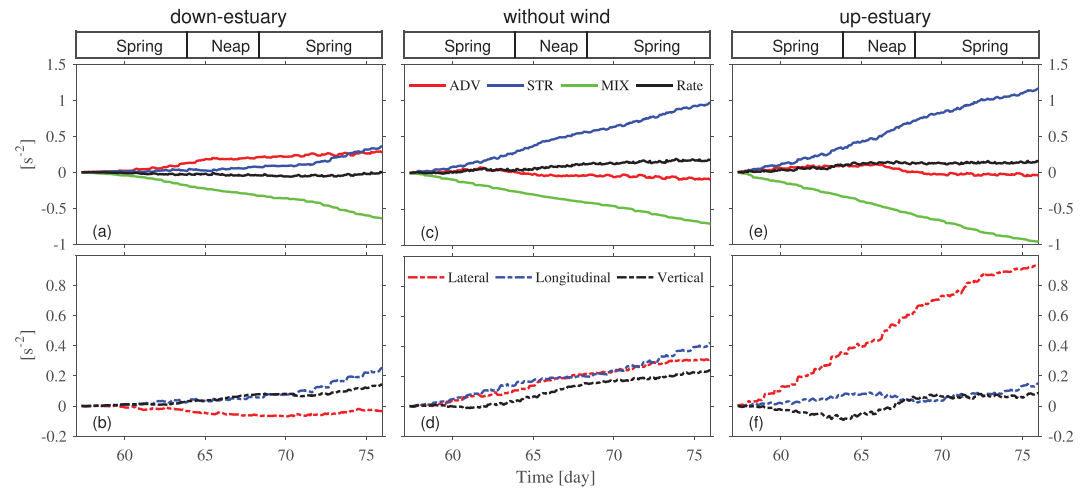
Figure 8. (a, c, e) Time series of the integrated terms and (b, d, f) time series of the integrated straining terms in different directions at the lower bay in the stratification equation: the advection (red solid), straining (blue solid), diffusion (green solid), time-change rate (black solid), longitudinal straining terms (blue dashed), lateral straining term (red dashed), and vertical straining term (black dashed), obtained from the down-estuary wind, without wind, and the up-estuary wind model runs. A positive value represents the tendency to increase stratification.

5.2.1. The Intrinsic Connection Between Density Stratification and Bottom Friction

As shown above, the density stratification exhibited a completely opposite response to axial winds in the upper and lower bays. Scully and Friedrichs (2007a) proposed that density stratification causes the bottom stress to deviate from the law of the wall relationship and the estuarine stratification could strongly influence the bottom stress. The bottom stress closely corresponded to these density stratification changes (Figure 10). In addition, the wind-driven currents can modify the bottom flow. The down-estuary winds enhances the bottom landward flow during flood tides and decreases the seaward flow during ebb tides, and vice versa. These changes in bottom flow would modulate the variation of bottom stress.

The down-estuary winds significantly decreased N^2 in the lower bay but slightly increased density stratification in the upper bay (Figure 10a). The bottom stress was strongly influenced by the wind-driven bottom flow and vertical stratification induced by axial winds. For instance, the down-estuary winds significantly decreased density stratification in the lower bay, promoted vertical momentum transfer, and increased bottom stress (Figure 10b). In the middle bay, the increment in bottom stress induced by stratification reduction and the decrement caused by wind-driven bottom flow offset each other, resulting in little change in the bottom stress (Figure 10b). In the upper bay, the increase in density stratification and decrease in bottom flow by the down-estuary winds worked together to reduce the bottom stress. These changes in the bottom stress were more distinct during spring tides than during the neap tide (Figure 10b).

Under the up-estuary winds, the complex competition between wind mixing and wind straining caused weakened stratification in the upper and middle bays and enhanced density stratification in the lower bay, especially during the neap tide (Figure 10d). The bottom stress showed an increase under decreased stratification and vice versa (Figure 10e). It is important to note that the increased bottom stress under the up-estuary winds usually occurred at peak ebbs because of the joint effects of stratification reduction and wind-driven bottom flow in the upper and middle bays (Figure 10e). For example, the up-estuary winds decreased the buoyancy frequency in the middle bay by nearly 0.015 rad^2 s^{-2} (Day 65, 22.05°N), significantly enhancing bottom stress by 0.19 Pa (Figure 10e). Because the increment in bottom stress was larger on ebbs than on floods, the up-estuary winds induced significant tidal asymmetries in bottom stress and sediment resuspension, leading to enhanced tidal oscillatory sediment transport or sediment pumping (Scully & Friedrichs, 2007a).

Along with the changes in the bottom stress, the seabed erosion/deposition endured corresponding variations. The down-estuary winds induced enhanced sediment deposition at the upper bay and bed erosion in the lower bay, especially during the neap tide (Figure 10c), consistent with the decreased bottom stress
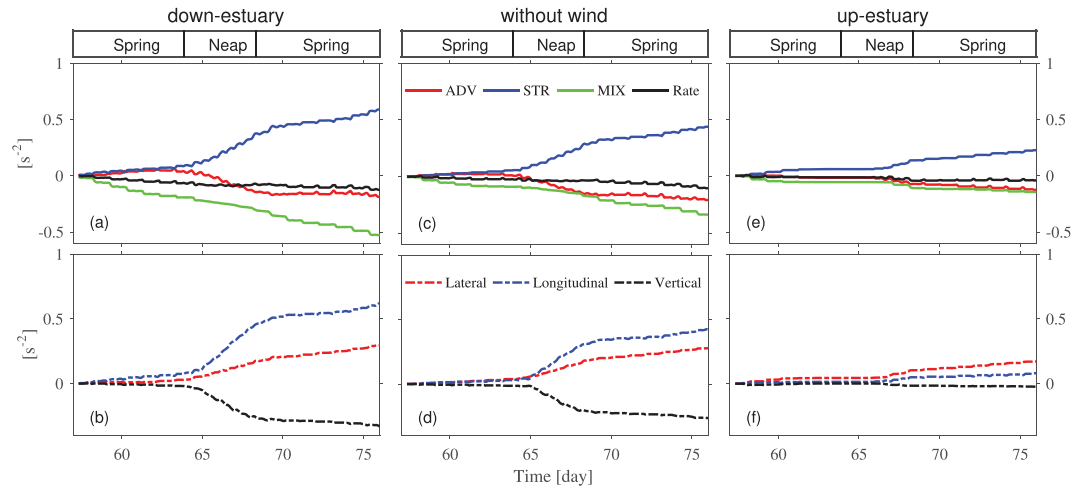
Figure 9. Same as Figure 8 but in the upper bay.

in the upper bay and the increased bottom stress in the middle and lower bays. Under the up-estuary winds, obvious bed erosion occurred at the middle and upper bays at the end of the first spring tide period and the first half of the neap tide (Figure 10f), which was consistent with the increment of bottom stress and the reduction in density stratification. During the second half of the neap tide, the seabed experienced deposition in the middle and lower bays but significant erosion in the upper bay, induced by the enhanced bottom friction in the upper bay and the weakened one in the middle and lower bays (Figure 10f). Generally, the effect of the down-estuary winds on seabed change was not as remarkable as that of the up-estuary winds.

5.2.2. The Tidal Oscillatory Flux

To demonstrate the basic mechanism of the axial winds altering tidal oscillatory sediment transport, the tidally averaged sediment flux at a chosen station in the upper bay (S13 in Figure 1b) was decomposed by adopting the decomposition method of Geyer et al. (2001), Scully and Friedrichs (2007a), and Becherer et al. (2016).

$$
\begin{aligned}
vC &= (v + v')(C + C') \\
&\left([v]_z + \widetilde{v} + v'\right)\left([C]_z + \widetilde{C} + C'\right) \\
&= \underbrace{[v]_z[C]_z}_{F_{bf}} + \underbrace{\widetilde{v}\left[\widetilde{C}\right]}_{F_{exf}} + \underbrace{v'C'}_{F_{tpf}}
\end{aligned}
\tag{3}
$$

where v is the axial velocity, C is the SSC, and z is the vertical coordinate. The prime and tilde symbols denote deviations from the tidally averaged value and vertical mean, respectively. The subscripts denote the direction in which a variable is considered. The angle and square brackets denote the tidal average and vertical mean, respectively. Tidally averaged sediment transport was decomposed into tidal pumping sediment flux (F_{tpf}) and advective sediment transport that includes a barotropic term (F_{bf}) and sediment flux due to the vertical exchange flow (F_{exf}).

Without wind forcing, there was a landward-directed bottom flow and seaward-directed surface flow in the subtidal velocity profile (Figure 11a). The barotropic flow component was a seaward-directed sediment flux that was offset by an exchange flow component and a tidal pumping component, resulting in landward net sediment transport during the neap tide (Figure 11g and Table 3). Under the up-estuary winds, the enhanced sediment resuspension during the peak ebb caused tidal asymmetries in sediment transport (Figure 11e), which significantly weakened the landward tidal pumping component and even generated a seaward-directed sediment flux (Figure 11j). However, the weakened density stratification also strongly decreased the vertical gradient of sediment (Figure 11e). Combined with the weakened current shear ($\frac{\partial v}{\partial z}$), it significantly reduced the landward exchange flow component by 86.0% (Figures 11b and 11e). In general,
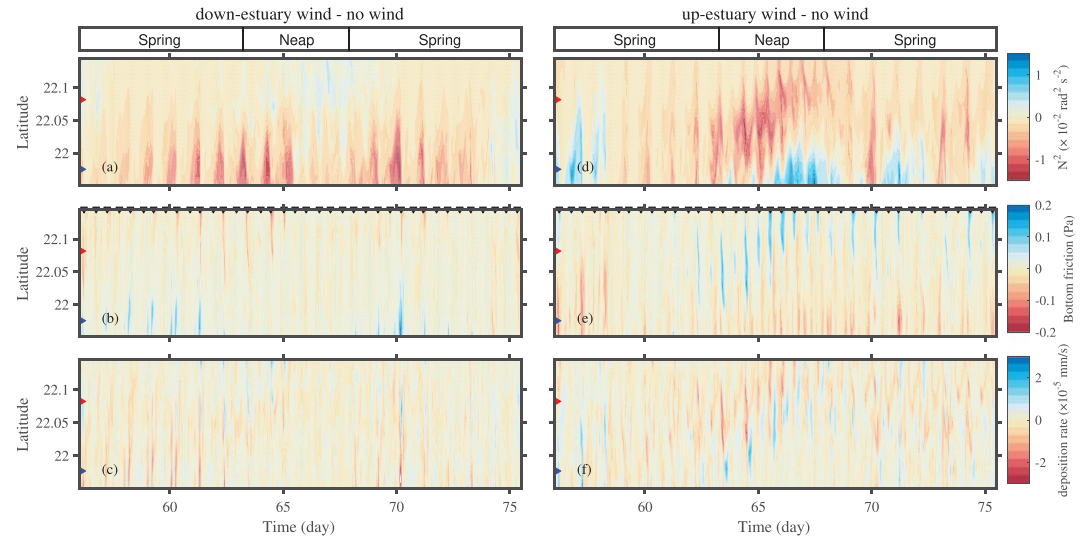
Figure 10. Time series of cross-channel integrated changes in (a, d) buoyancy frequency, (b, e) bottom friction, and (c, f) deposition rate obtained by subtracting that without wind from the runs under down-estuary wind and up-estuary wind. Positive deposition rate denotes sediment deposition and tends to increase bed thickness, while negative deposition rate represents bed erosion. The inverted triangles on the upper axis of (b) and (e) represent the time of maximum ebb tide. The red (blue) triangle on the left axis represents the junction between the upper and middle bays (the middle and lower bays).

almost half of the seaward net sediment transport induced by the up-estuary winds was caused by tidal asymmetries in sediment resuspension, whereas the other half was due to the stratification reduction that influenced the vertical distribution of SSC. Tidal asymmetries in sediment resuspension was mainly caused by tidal asymmetries in bottom stress. The down-estuary winds slightly decreased the landward barotropic flow component, the seaward exchange flow component, and the tidal pumping component because the effect of down-estuary winds on the vertical shear and vertical distribution of sediment was less remarkable than that of the up-estuary winds.

5.2.3. SSC Flux Decomposition

The result from the above decomposition suggests that sediment pumping induced by axial winds, especially the up-estuary winds, was generated by tidal asymmetries in sediment resuspension. This asymmetry arose owing to tidal asymmetries in density stratification and bottom stress, which were induced by the joint effects of tidal straining and wind straining. To investigate how this mechanism influences longitudinal residual sediment transport, we decomposed the longitudinal sediment transport by adopting a sediment flux decomposition method proposed by several authors (Fischer, 1972; Uncles et al., 1985; Lerczak et al., 2006; Scully & Friedrichs, 2007a; Chen & Sanford, 2009a; Burchard et al., 2018). The tidally averaged suspended sediment transport at a cross section can be decomposed into five components.

$$F_s = \underbrace{W\left[D[vC]_z\right]_x}_{T}$$

$$= \underbrace{W\left[D[v]_z[C]_z\right]_x}_{T_1} + \underbrace{W[D[v]'_z[C]'_z]_x}_{T_2} + \underbrace{W\left[D\left[\widetilde{v}\widetilde{C}\right]_z\right]_x}_{T_3} \ (4)$$

$$+ \underbrace{W\left[D\left[\widetilde{v}'\widetilde{C}'\right]_z\right]_x}_{T_4} + \underbrace{W[D'[vC]'_z]_x}_{T_5},$$

where W is the width of the cross section, D is the water depth, T_1 represents the sediment flux resulting from runoff or barotropic flows, T_2 represents the tidal oscillatory sediment flux, T_3 represents the sediment flux driven by subtidal exchange flow or subtidal shear dispersion, T_4 is the combined temporal and vertical covariance transport, and T_5 is the water depth covariance with velocity and SSC or Stokes transport.
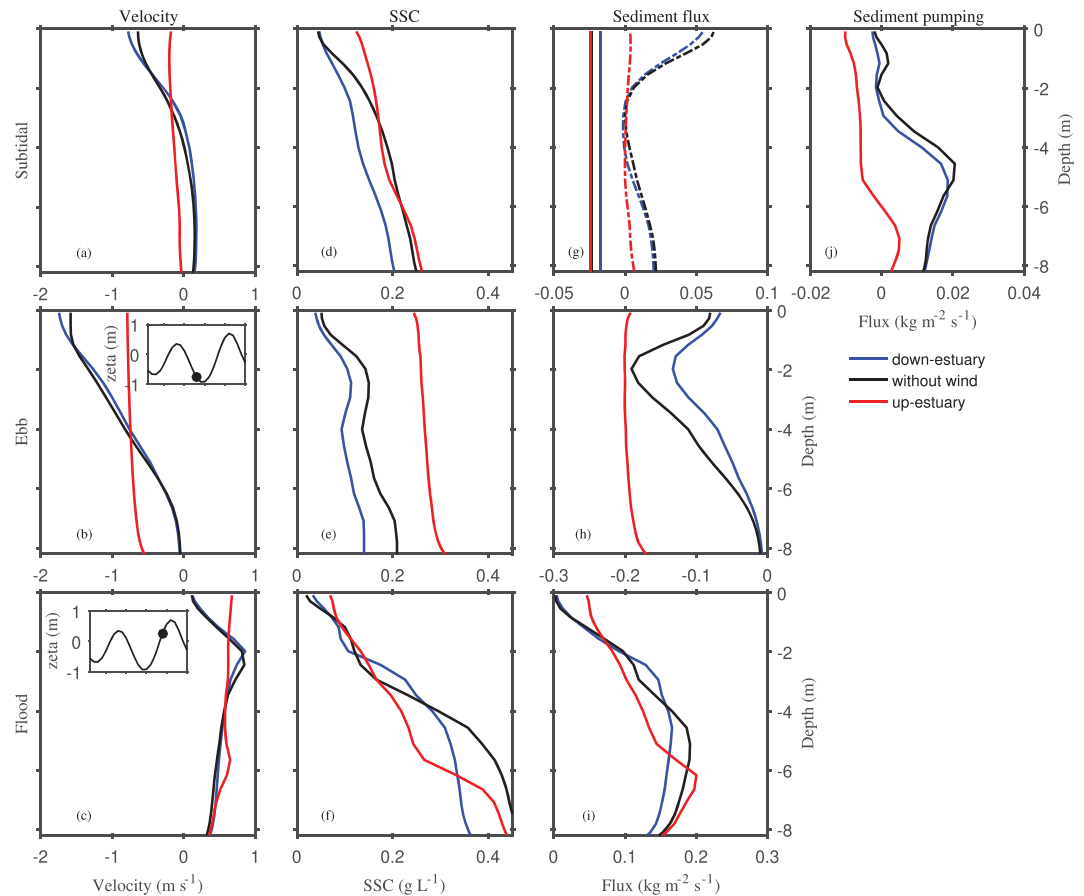
Figure 11. The tidally averaged profiles of (a) along-channel velocity; (d) SSC; and instantaneous profiles of (b, c) along-channel velocity, (e, f) SSC, and (h, i) sediment flux at a station in the channel on Sec. B for ebb and flood during the neap tide (Day 66). Tidally averaged sediment transport is decomposed into (j) sediment pumping and (g) advective sediment transport that includes barotropic term (solid line) and sediment flux due to the vertical exchange flow (dashed line). Positive velocity or sediment flux denotes up-estuary (northward) transport. The black dots in (b) and (c) represent the peak ebb and the peak flood, respectively.

The decomposition of sediment transport fluxes shows that changes in T_1, T_4, and T_5 by axial wind forcings were generally negligible (changes in T_4 and T_5 are typically less than 20 kg s^{-1} and that in T_1 was generally less than 100 kg s^{-1}; Figures 12a, 12d, 12e, 12g, 12j, and 12k). In contrast, the changes in the tidal oscillatory sediment flux (T_2) were considerable and responded almost linearly to the variation of bottom stress (Figures 12b and 12h). Generally, the down-estuary winds increased the seaward transport of T_2, especially at the lower bay during spring tides (Figure 12b), with correspondingly obvious enhanced bottom stress on ebbs in the lower bay (Figure 10b). During the stratified neap tide, the changes in the tidal oscillatory sediment flux (T_2) were less remarkable, probably due to the small changes in bottom stress (Figure 12h). The up-estuary winds generated a strong seaward residual sediment transport of T_2 and reached a maximum of -394.7 kg s^{-1} on Day 65 (nearly 22.05°N) (Figure 12h), which is consistent with the peak time of the increment of bottom stress (Figure 10e). Overall, the spatiotemporal variation of T_2 was strongly correlated with the changes in density stratification and bottom stress (Figures 10d, 10e, and 12h).

The down-estuary winds had little effect on the subtidal shear transport (T_3) (Figure 12c), which is consistent with little changes in the vertical shear and vertical distribution of the SSC under the down-estuary winds (Figures 11a–11f). However, the up-estuary winds reduced the landward subtidal shear (T_3) during the neap tide (Figure 12i) because the up-estuary winds significantly decreased the estuarine stratification in the upper bay, which strongly influenced the vertical distribution of SSC (Figure 11e).

Table 3
The Vertically Integrated Decomposition Results of Tidally Averaged Sediment Flux at S5 on Day 66

Sediment flux	F_{bf} (kg m^{-2} s^{-1})	F_{exf} (kg m^{-2} s^{-1})	F_{tpf} (kg m^{-2} s^{-1})
Down-estuary	−0.142	0.113	0.069
No wind	−0.195	0.136	0.079
Up-estuary	−0.199	0.019	−0.029

The above analysis demonstrates that axial winds affected sediment transport partly by altering vertical stratification and the vertical distribution of the SSC and thus changing the associated subtidal shear dispersion (T_3), partly by inducing an asymmetry in bed stress and changing the tidal oscillatory sediment flux (T_2), and partly by the direct impact of the wind-driven barotropic flow, thus changing the advective component (T_1). We stress that the down-estuary winds had a relatively minor impact on sediment flux, whereas the up-estuary winds strongly enhanced seaward sediment transport mainly through the increased seaward tidal oscillatory flux (T_2) and decreased landward subtidal shear transport (T_3).

5.3. A conceptual Diagram

We use the Kelvin number, *Ke*, to represent the relative importance of the Earth's rotation in both the upper bay and the lower bay (Garvine, 1995; Li & Li, 2011; Valle-Levinson, 2008).

$$Ke = \frac{fB}{\sqrt{g'h_s}}, \tag{5}$$

where *B* is the estuary width, *f* is the Coriolis parameter, *g′* is the reduced gravitational acceleration, and h_s is the mean depth of the surface layer.

A conceptual diagram of how the vertical stratification responds to down- and up-estuary winds in a convergent estuary is illustrated in Figure 13. Because the transverse section is relatively narrow in the upper bay
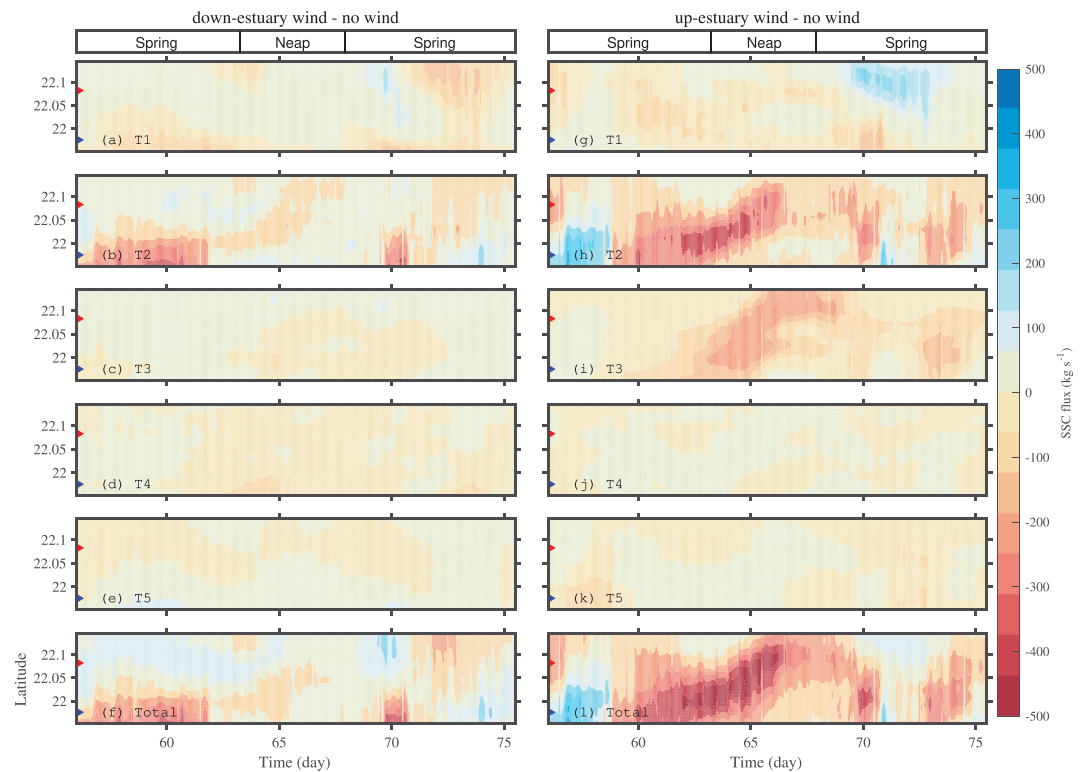

Figure 12. Time series of cross-sectionally integrated residual sediment transport due to (a, g) barotropic flows (T_1), (b, h) tidal oscillatory (T_2), (c, i) subtidal shear dispersion (T_3), (d, j) the combined temporal and vertical covariance transport (T_4), (e, k) stokes transport (T_5), and (f, l) total residual sediment transport obtained by subtracting that without wind from the runs of down-estuary wind and up-estuary wind. The increase in seaward (landward) residual sediment transport due to each term is shown in red (blue). The red (blue) triangle on the left axis represents the junction between the upper and middle bays (the middle and lower bays).
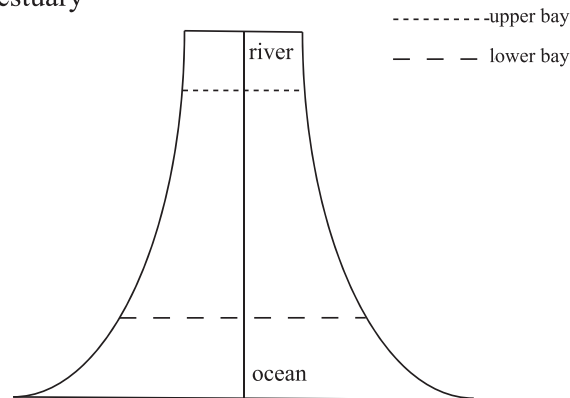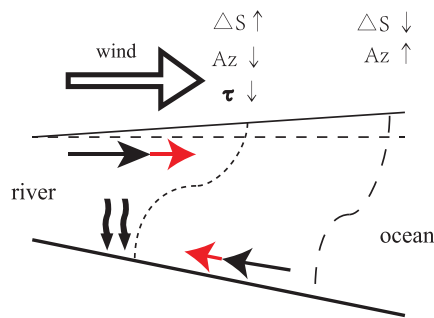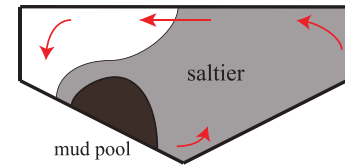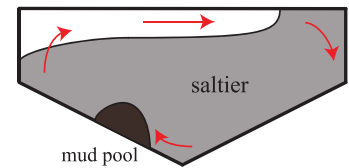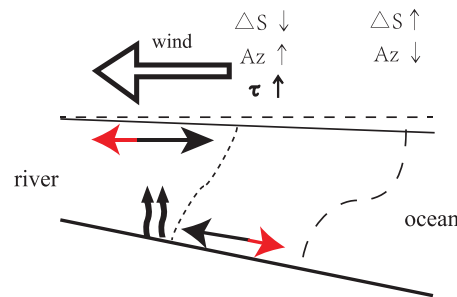
Figure 13. Conceptual diagram to illustrate the effects of axial winds at a convergent estuary. The lateral wind-driven circulation is marked by red thin arrows, the gravitational circulation (subtidal flow without wind forcing) is marked by black thick arrows, and the along-channel wind-driven circulation is marked by red thick arrows. The locations and salinity vertical distribution of the upper bay and the lower bay are marked by small-interval dashed line and large dashed line, respectively. S and τ are the surface-to-bottom salinity difference and bottom friction, respectively. Az denotes the depth-averaged vertical eddy diffusivity.

($Ke \approx 0.2$), the wind-driven lateral circulation and wind lateral straining are negligible compared to the longitudinal ones. Under the up-estuary wind, the vertical shear in the longitudinal direction ($\frac{\partial v}{\partial z}$) is significantly weakened, acting on the along-channel salinity gradient ($\frac{\partial S}{\partial y}$) and resulting in a great stratification reduction (Figure 13c). When forced by the down-estuary wind, the term $\frac{\partial v}{\partial z}$ is enhanced (Figure 13b). When acting on the along-channel salinity gradient ($\frac{\partial S}{\partial y}$), it stratifies the water column. In the lower bay ($Ke \approx 0.9$), the lateral circulation driven by the up-estuary wind is much stronger than that in the upper bay. The wind-driven lateral circulation significantly enhances the vertical shear of the lateral flow ($\frac{\partial u}{\partial z}$) and slightly weakens the

lateral salinity gradient ($\frac{\partial S}{\partial x}$), leading to an increment in lateral straining effect and an increase in density stratification. However, the down-estuary wind reduces or even reverses the subtidal vertical shear of the lateral flow ($\frac{\partial u}{\partial z}$), which strains the lateral salinity gradient ($\frac{\partial S}{\partial x}$), resulting in a stratification reduction. In the lower wide bay, the lateral wind straining obviously overwhelms the longitudinal wind straining, which induces a stratification reduction under the up-estuary wind and a stratification increment under the down-estuary wind.

In a word, the stratification change responding to axial winds is largely modulated by the competitions among along-channel wind straining, cross-channel wind straining, and direct wind-driven mixing. Chen and Sanford (2009a) demonstrated that longitudinal current and the along-channel straining were much stronger in a narrow, partially mixed estuary; thus, the competition between the along-channel wind straining and wind-driven mixing controlled the stratification change. This pattern is also applicable to the narrow upper bay (low Ke) of a convergent estuary but not applicable to the wide lower bay. The lateral current and lateral straining are stronger than the longitudinal ones in the lower bay, as proposed by Xie and Li (2018).

The sediment dynamic analyzed above demonstrates that changes in sediment transport are associated with changes in estuarine stratification responding to different axial winds. Under the up-estuary wind, the joint effect of wind straining and tidal straining on the longitudinal salinity gradient significantly reduces density stratification during peak ebbs in the upper bay and thus enhances turbulent mixing, promotes vertical momentum transfer, and increases bottom friction, resulting in greater sediment resuspension on ebbs and an enhanced tidal asymmetry in SSC during a tidal cycle and therefore a larger seaward sediment pumping (T_2). Additionally, seaward flow at the bottom induced by the up-estuary wind amplifies the near-bed seaward flow during ebbs, thus generating larger bed stresses than at floods. The tidal asymmetry in bed stress generates tidal asymmetry in sediment resuspension and increases sediment pumping (T_2). On the other hand, the up-estuary wind reduces density stratification, vertical current shear, and the vertical gradient of SSC in the upper bay; thus, it decreases the subtidal shear transport (T_3). This effect is more distinct during neap tides. The down-estuary wind has no notable impact on longitudinal sediment transport; however, it does enhance sediment entrapment at the upper estuary by increasing estuarine stratification and decreasing bottom friction and seabed resuspension.

6. Summary and Conclusions

In this study, we used the COAWST modeling system to investigate the effect of axial winds on the vertical stratification and suspended sediment transport in a funnel-shaped estuary in the wet season. We compared the results of model runs without wind and with up- and down-estuary winds and analyzed the changes in longitudinal and lateral currents, salinity, SSC, and vertical stratification. We also explored the mechanisms for changes in vertical stratification in the upper and lower bays by diagnostic analysis of the stratification equation. The time variation of vertical stratification was decomposed into three components: advection, straining, and diffusion. The changes in stratification and bottom friction were investigated and used to explain the wind effect on sediment transport fluxes.

Our results indicate that the vertical stratification is typically balanced by the straining term and the diffusion term. The diagnostic results show that vertical stratification in the upper bay ($Ke \approx 0.2$), where wind-driven lateral circulation is weak, significantly decreases/increases under the up-estuary/down-estuary winds owing to longitudinal wind straining, which enhances/weakens subtidal vertical shear and the strength of the exchange flow correspondingly. For the lower bay ($Ke \approx 0.9$), the lateral wind straining offsets the longitudinal wind straining and increases stratification during the up-estuary wind and decreases stratification under the down-estuary wind.

For sediment dynamics, the down-estuary wind exhibits no obvious effects on sediment flux, whereas the up-estuary wind contributes to a strong seaward sediment flux owing to the reduced landward tidal oscillatory flux and a weakened landward sediment flux due to subtidal shear dispersion, both of which are associated with changes in density stratification. The tidal oscillatory flux is most affected by the axial winds, whereas the subtidal shear dispersion is less affected, except during neap tides. Influenced by the up-estuary winds, the bottom friction is enhanced on ebbs, which is caused by the wind-driven

bottom seaward flow and the decreased stratification due to the joint effect of wind straining and tidal straining, and generates asymmetry in sediment resuspension, resulting in an increased seaward tidal oscillatory flux. Meanwhile, the up-estuary winds enhance vertical mixing and drive lateral circulation in the upper bay, which transport sediment from the lower-energy bottom layer to the higher-energy surface layer, resulting in a seaward sediment flux.

As our study did not consider wave mixing or other wave effects, some discrepancies between our model results and real sediment transport would occur. Previous observations (Baker & Lavelle, 1984; Brand et al., 2010; Sanford, 1994) showed that wind waves enhance resuspension in the shallow regions where waves interact with the sea floor. A future study with wave effects will be conducted in the HE. Additionally, different geometries with variable convergence will be examined to make this study more universal.

Appendix A

There have been several short-term field measurements conducted in the Huangmaohai Estuary (HE) (Gong et al., 2014). As our study is mainly focused on hydrodynamics and sediment transport during wet seasons, we selected two field measurements to validate our model, including 27–28 June 2010 and 2–4 July 2012. On 27–28 June 2010, four stations were deployed in the HE, and hourly measurements were taken for current,
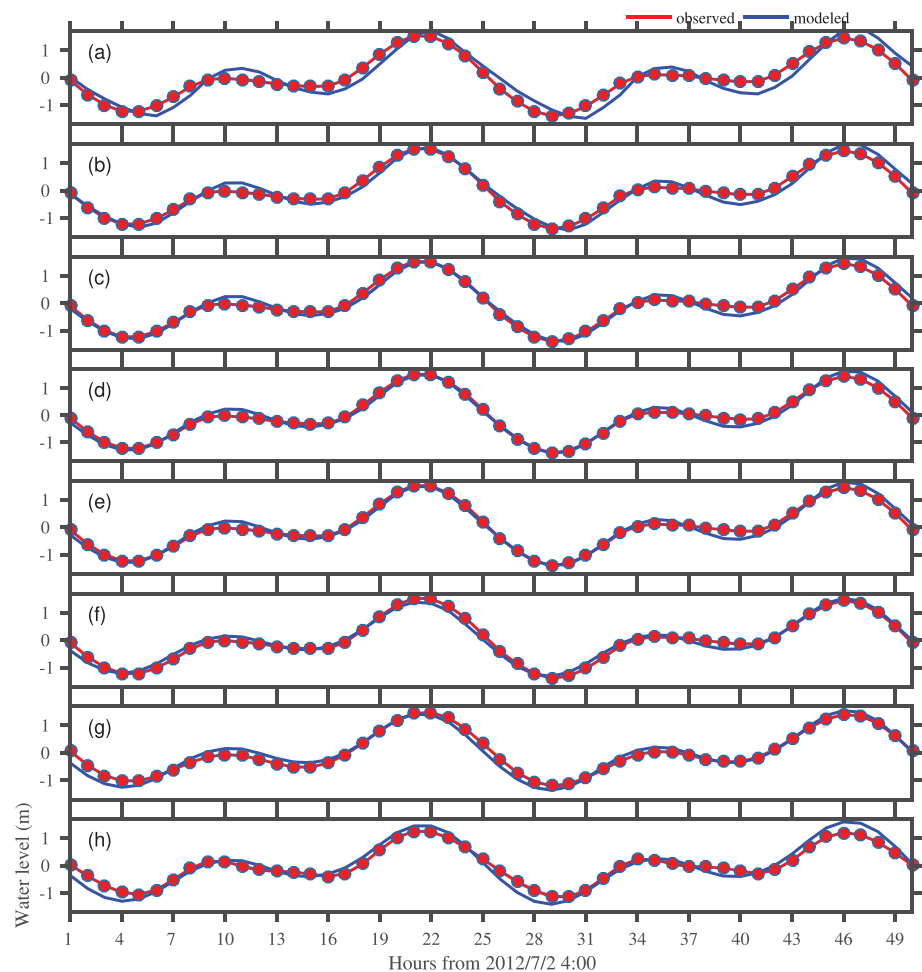

Figure A1. Validation of water levels at (a–h) S5–S12. Red lines with dots for the observation, and blue lines for the model results.

Table A1
Validation Results of Water Elevation, Current, Salinity, and Suspended Sediment Concentration

		S1	S2	S3	S4	S5	S6	S7	S8	S9	S10	S11	S12
Water elevation (m)	(RMSE)	0.30	0.37	0.20	0.23	0.31	0.19	0.15	0.14	0.13	0.13	0.17	0.23
	(SK)	0.95	0.94	0.98	0.97	0.97	0.99	0.99	0.99	0.99	0.99	0.99	0.98
Velocity (m s^{-1})	Sur (RMSE)	0.2	0.27	0.33	0.36	0.46	0.32	0.37	0.30	0.28	0.31	0.27	0.34
	Sur (SK)	0.86	0.92	0.93	0.92	0.89	0.94	0.88	0.94	0.92	0.87	0.92	0.70
	Mid (RMSE)	0.18	0.25	0.33	0.29	0.41	0.31	0.24	0.25	0.24	0.21	0.21	0.22
	Mid (SK)	0.87	0.93	0.92	0.92	0.90	0.93	0.93	0.94	0.93	0.92	0.94	0.88
	Bot (RMSE)	0.17	0.2	0.31	0.27	0.38	0.26	0.36	0.32	0.20	0.24	0.18	0.19
	Bot (SK)	0.87	0.94	0.89	0.83	0.88	0.93	0.56	0.74	0.93	0.79	0.92	0.78
Salinity (psu)	Sur (RMSE)	0	0	0.55	3.97	0.18	0.93	1.26	2.35	3.20	3.81	5.27	2.94
	Sur (SK)	a	-	0.41	0.75	-	0.63	0.51	0.66	0.71	0.31	0.43	0.53
	Mid (RMSE)	0.02	0.02	1.74	4.72	0.18	0.69	3.73	4.07	4.24	5.55	6.56	5.05
	Mid (SK)	-	-	0.74	0.71	-	0.94	0.73	0.86	0.66	0.45	0.57	0.46
	Bot (RMSE)	0	0	3.55	4.41	0.18	1.45	3.51	2.59	4.82	7.20	4.96	6.02
	Bot (SK)	-	-	0.73	0.81	0.00	0.89	0.80	0.95	0.63	0.62	0.72	0.59
SSC (g L^{-1})	Sur (RMSE)	0.03	0.03	0.07	0.12	0.08	0.12	0.10	0.12	0.13	0.02	0.05	0.02
	Sur (SK)	0.66	0.6	0.74	0.51	0.40	0.48	0.73	0.82	0.64	0.37	0.19	0.70
	Mid (RMSE)	0.02	0.03	0.06	0.16	0.07	0.11	0.08	0.15	0.12	0.03	0.08	0.05
	Mid (SK)	0.58	0.79	0.81	0.6	0.60	0.65	0.79	0.77	0.75	0.51	0.15	0.42
	Bot (RMSE)	0.03	0.05	0.05	0.14	0.08	0.11	0.10	0.14	0.11	0.02	0.07	0.07
	Bot (SK)	0.55	0.77	0.73	0.77	0.53	0.73	0.70	0.81	0.83	0.75	0.40	0.39

Abbreviations: RMSE, root mean square error; SK, Willmott skill score; SSC, suspended sediment concentration.
[a]*Because the bias of model and observation is too small (almost to 0), the Willmott skill score is also small and we do not present the skill score.*
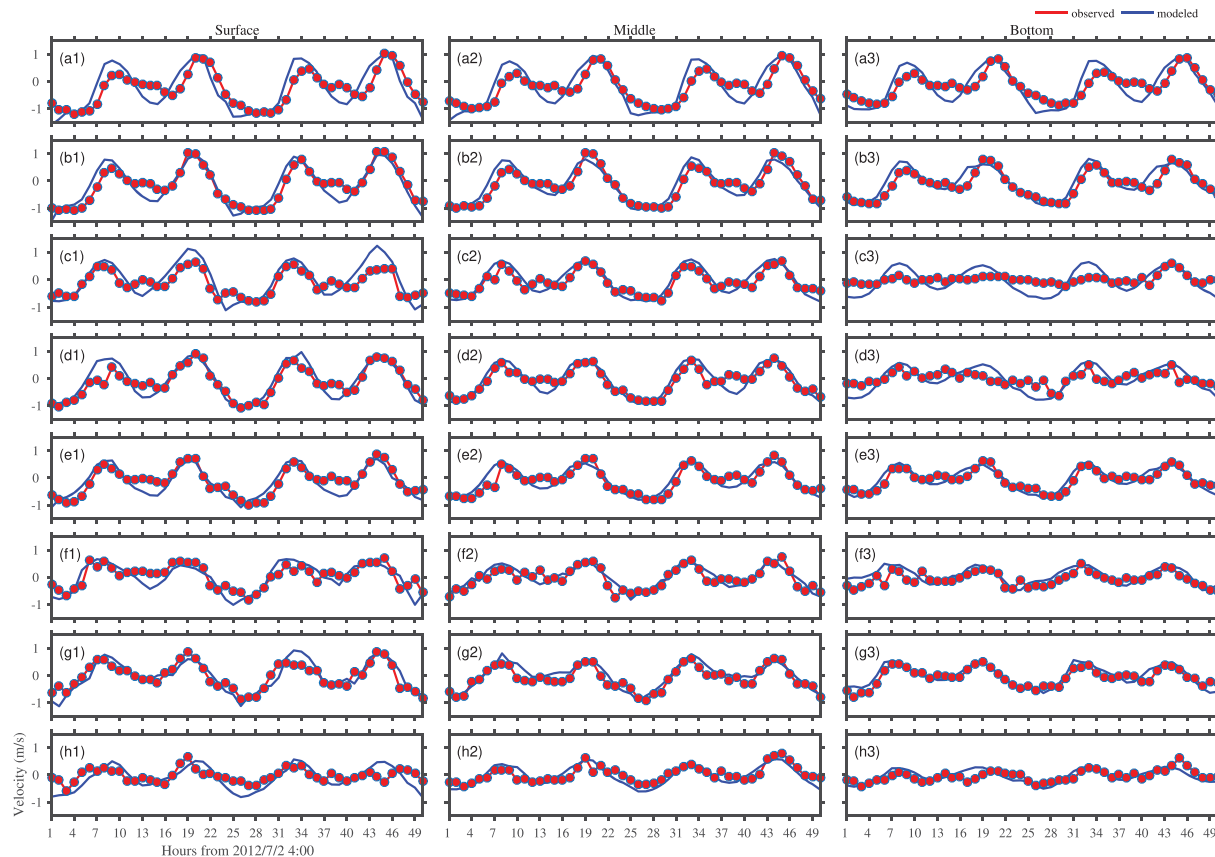

Figure A2. Validation of along-chanel flows at (a–h) S5–S12. The current (left column) at the surface and (right column) for the bottom. (middle) For the middle layer. Red lines are for the observation, and blue lines for the model results. The positive for axial flows means landward.
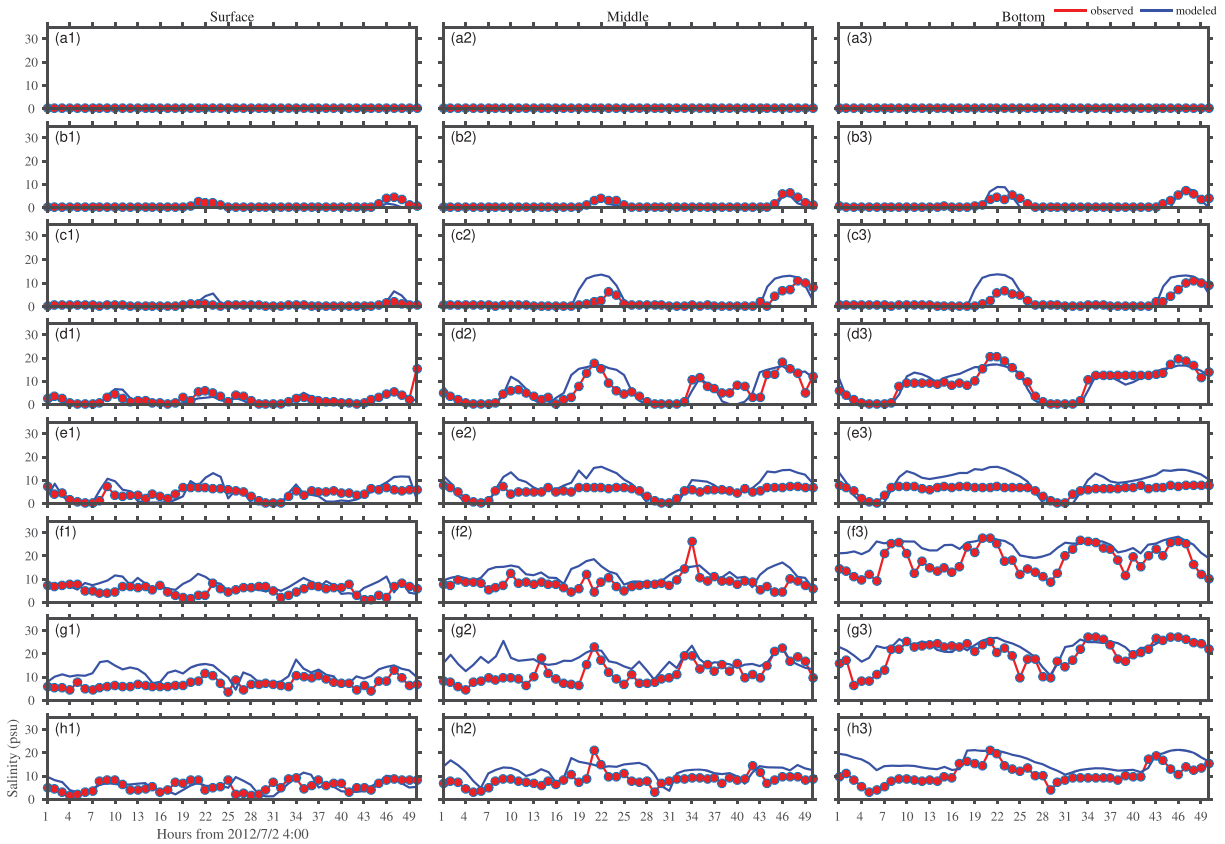
Figure A3. Validation of salinity at (a–h) S5–S12. Red lines are for the observation, and blue lines for the model results.

salinity, and suspended sediment concentration (SSC) profiles for a 28-hr duration (the black dots [S1–S4] in Figure A1b). The current and salinity profiles were obtained by direct-reading current meters (SL9-2) and CTDs, respectively. Water samples were collected hourly from six vertical layers (surface, 0.2H, 0.4H, 0.6H, 0.8H, and bottom layers) and subjected to laboratory analysis to estimate the SSC (filtering, drying, and weighing). The field work on 2–4 July 2012 consisted of eight stations to measure the current, salinity, and SSC profiles for a 50-hr duration (the red dots [S5–S12] in Figure A1b). The current and SSC profiles were measured by down-looking acoustic Doppler current profilers and optical backscatter sensor (Model OBS-3A), respectively. More details about the field campaigns are in Gong et al. (2014).

We ran two model simulations, one from 16 April to 1 July 2010 (76 days) and the other from 16 April to 15 July 2012 (90 days), to separately validate the model by these extensive field measurement data. For the sake of space, the details of validation in 2010 are not shown here, but the model performance indices are shown in Table A1.

The accuracy of model results is quantified by the root mean square error (RMSE) and the Willmott skill score (Willmott, 1981), which are defined as

$$\text{RMSE} = \sqrt{\frac{1}{n}\sum_{i=1}^{n}(O_i - M_i)^2},\tag{A1}$$

$$\text{SK} = 1 - \frac{\sum_{i=1}^{n}(O_i - M_i)^2}{\sum_{i=1}^{n}\left[|M_i - \overline{O}| + |O_i - \overline{O}|\right]^2},\tag{A2}$$

where n is the number of observations and M_i and O_i are the model result and the observation, respectively. The overbar is for the mean value.
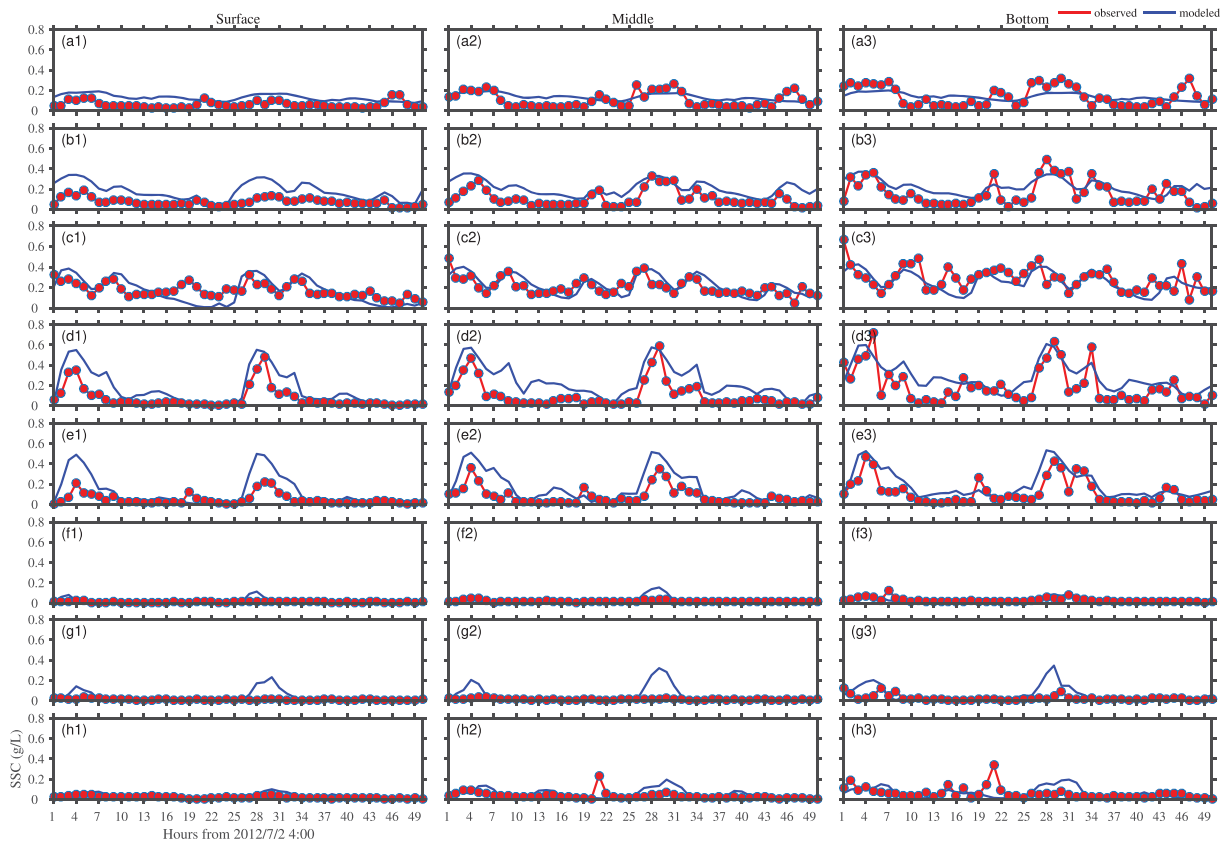
Figure A4. Validation of SSC at (a–h) S5–S12. Red lines with dots are for the observation, and blue lines for the model results.

A.1. Water level

As shown in Figure A1a and Table A1a, the comparison between modeled and observed water elevations indicated that the model could well reproduce the water level. In 2010, the RMSEs and skill scores were generally less than 0.3 m and larger than 0.94, respectively. In 2012, the modeled water levels showed better agreement with the observed water levels, with averaged RMSEs < 0.18 m and skill scores > 0.98. However, the discrepancy increased in the upstream direction from the estuary mouth (e.g., S1, S2, and S5), similar to the validation result by Gong et al. (2016). This discrepancy may be induced by inaccurate bathymetry at the upper bay and underestimation of upstream runoff by the parent model.

A.2. Water current

We examine the model performance in simulating water currents at surface, middle, and bottom layers (Figure A2a). In 2010, the modeled results showed good agreement with the observations, and the averaged RMSE and skill score of currents at three layers for all stations were 0.26 m s^{-1} and 0.9, respectively (Table A1). The discrepancy of current simulation typically occurred at the peak flood/ebb times, and the RMSEs at bottom are less than those at the surface. In 2012, the averaged RMSE and skill score of water current over eight stations were 0.29 m s^{-1} and 0.88, respectively. The overestimate at S8 was probably owing to the bathymetric inaccuracy of the child model on the west shoal. Generally, the velocity fluctuations of the modeled flow were smoother than those measured.

A.3. Salinity and SSC

The averaged skill scores of salinity and SSC at the selected stations were 0.66 and 0.62, respectively (Table A1). Additionally, the averaged RMSEs of salinity and SSC at three vertical layers over all stations were 2.7 psu and 0.08 g L^{-1}, respectively, indicating that the model can reasonably reproduce the salinity and SSC. Influenced by strong upstream runoff during the wet seasons, the RMSEs of salinity at S1, S2, and S5 were almost 0. At other stations, the model slightly overestimated the salinity but captured well

the phases of salinity variations (Figure A3a). For the suspended sediment, the model slightly underpredicted the SSC in the bottom layers but overestimated the SSC in the surface layers at the selected stations (Figure A4a). The poor performances at S10–12 were probably attributed to the inaccuracy in grain-size distribution owing to sparse direct observations there. Furthermore, the inaccuracy in SSC at open boundaries was another influencing factor. Chen et al. (2017) proposed that the dispersal of the Pearl River plume over continental shelf would deliver sediment from the Pearl River Estuary to the child model domain, making it difficult to set accurate SSCs at open boundaries from the parent model.

There were other two reasons for the discrepancies in simulating salinity and SSC. First, because the bathymetry in the river network in the Pearl River Delta changed significantly due to both natural processes and anthropogenic activities (Zhang et al., 2010), and the river discharges from these distributaries varied greatly in space and time; it is difficult to accurately capture the river inflows and riverine SSC into the HE. Second, the sediment distribution in the seabed specified in the model might not exactly represent the real situation because sediment fractions varied greatly by extreme weather events and human activities such as waterway dredging, although we made great efforts to improve it. As a whole, the model performed reasonably well in reproducing the hydro and sediment dynamics in the HE.

References

Allen, G. P., Salomon, J. C., Bassoullet, P., Du Penhoat, Y., & de Grandpré, C. (1980). Effects of tides on mixing and suspended sediment transport in macrotidal estuaries. *Sedimentary Geology*, *26*(1–3), 69–90. https://doi.org/10.1016/0037-0738(80)90006-8

Baker, E. T., & Lavelle, J. W. (1984). Effect of particle size on the light attenuation coefficient of natural suspensions. *Journal of Geophysical Research*, *89*(C5), 8197–8203. https://doi.org/10.1029/JC089iC05p08197

Becherer, J., Flöser, G., Umlauf, L., & Burchard, H. (2016). Estuarine circulation versus tidal pumping: Sediment transport in a well-mixed tidal inlet. *Journal of Geophysical Research: Oceans*, *121*(8), 6251–6270. https://doi.org/10.1002/2016JC011640

Blumberg, A. F. (2002). A primer for ECOMSED version 1.3 user manual. Technical Report, HydroQual, Inc., Mahwah, New Jersey.

Brand, A., Lacy, J. R., Hsu, K., Hoover, D., Gladding, S., & Stacey, M. T. (2010). Wind-enhanced resuspension in the shallow waters of South San Francisco Bay: Mechanisms and potential implications for cohesive sediment transport. *Journal of Geophysical Research*, *115*(11), 1–15. https://doi.org/10.1029/2010JC006172

Burchard, H., Schuttelaars, H. M., & Ralston, D. K. (2018). Sediment trapping in estuaries. *Annual Review of Marine Science*, *10*(1), annurev-marine-010816-060535 https://doi.org/10.1146/annurev-marine-010816-060535

Chant, R. J. (2002). Secondary circulation in a region of flow curvature: Relationship with tidal forcing and river discharge. *Journal of Geophysical Research*, *107*(C9), 3131. https://doi.org/10.1029/2001JC001082

Chant, R. J. (2007). Estuarine secondary circulation. In A. Valle-Levinson (Ed.), *Contemporary issues in estuarine physics* (Vol. 136, pp. 100–124). Cambridge: Cambridge University Press. https://doi.org/10.1017/CBO9780511676567.006

Chapman, D. C. (1985). Numerical treatment of cross-shelf open boundaries in a barotropic coastal ocean model. *Journal of Physical Oceanography*. https://doi.org/10.1175/1520-0485(1985)015<1060:NTOCSO>2.0.CO;2

Chen, S.-N., & Sanford, L. P. (2009a). Axial wind effects on stratification and longitudinal salt transport in an idealized, partially mixed estuary. *Journal of Physical Oceanography*, *39*(8), 1905–1920. https://doi.org/10.1175/2009JPO4016.1

Chen, Z., Gong, W., Cai, H., Chen, Y., & Zhang, H. (2017). Dispersal of the Pearl River plume over continental shelf in summer. *Estuarine, Coastal and Shelf Science*, *194*, 252–262. https://doi.org/10.1016/j.ecss.2017.06.025

Cheng, P., Li, M., & Li, Y. (2013). Generation of an estuarine sediment plume by a tropical storm. *Journal of Geophysical Research: Oceans*, *118*(2), 856–868. https://doi.org/10.1002/jgrc.20070

Cheng, P., Wang, A., & Jia, J. (2017). Analytical study of lateral-circulation-induced exchange flow in tidally dominated well-mixed estuaries. *Continental Shelf Research*, *140*(February 2016), 1–10. https://doi.org/10.1016/j.csr.2017.03.013

Cheng, P., & Wilson, R. E. (2008). Modeling sediment suspensions in an idealized tidal embayment: Importance of tidal asymmetry and settling lag. *Estuaries and Coasts*, *31*(5), 828–842. https://doi.org/10.1007/s12237-008-9081-4

Chernetsky, A. S., Schuttelaars, H. M., & Talke, S. A. (2010). The effect of tidal asymmetry and temporal settling lag on sediment trapping in tidal estuaries. *Ocean Dynamics*, *60*(5), 1219–1241. https://doi.org/10.1007/s10236-010-0329-8

de Jorge, V. N., & van Beusekom, J. E. E. (1995). Wind- and tide-induced resuspension of sediment and microphytobenthos from tidal flats in the Ems estuary. *Limnology and Oceanography*, *40*(4), 776–778. https://doi.org/10.4319/lo.1995.40.4.0776

Fischer, H. B. (1972). Mass transport mechanisms in partially stratified estuaries. *Journal of Fluid Mechanics*, *53*(4), 671–687. https://doi.org/10.1017/S0022112072000412

Flather, R. A., & Davies, A. M. (1976). Note on a preliminary scheme for storm surge prediction using numerical models. *Quarterly Journal of the Royal Meteorological Society*, *102*(431), 123–132. https://doi.org/10.1002/qj.49710243110

Garrett, C., MacCready, P., & Rhines, P. (1993). Boundary mixing and arrested Ekman layers: Rotating stratified flow near a sloping boundary. *Annual Review of Fluid Mechanics*, *25*(1), 291–323. https://doi.org/10.1146/annurev.fl.25.010193.001451

Garvine, R. W. (1995). A dynamical system for classifying buoyant coastal discharges. *Continental Shelf Research*, *15*(13), 1585–1596. https://doi.org/10.1016/0278-4343(94)00065-U

Gelfenbaum, G., & Smith, J. D. (1986). Experimental evaluation of a generalized suspended-sediment transport theory. In R. J. Knight & J. R. McClean (Eds.), *Shelf Sands and Sandstones, Memoir II* (pp. 133–144). Calgary: Canadian Society of Petroleum Geologists.

George, D. A., Largier, J. L., Storlazzi, C. D., Robart, M. J., & Gaylord, B. (2018). Currents, waves and sediment transport around the headland of Pt. Dume, California. *Continental Shelf Research*, *171*(October 2017), 63–76. https://doi.org/10.1016/j.csr.2018.10.011

Geyer, W. R., Woodruff, J. D., & Traykovski, P. (2001). Sediment transport and trapping in the Hudson River estuary. *Estuaries*, *24*(5), 670. https://doi.org/10.2307/1352875

Gong, W., Jia, L., Shen, J., & Liu, J. T. (2014). Sediment transport in response to changes in river discharge and tidal mixing in a funnel-shaped micro-tidal estuary. *Continental Shelf Research*, *76*(March), 89–107. https://doi.org/10.1016/j.csr.2014.01.006

Gong, W., Schuttelaars, H., & Zhang, H. (2016). Tidal asymmetry in a funnel-shaped estuary with mixed semidiurnal tides. *Ocean Dynamics*, *66*(5), 637–658. https://doi.org/10.1007/s10236-016-0943-1

Grasso, F., Verney, R., Le Hir, P., Thouvenin, B., Schulz, E., Kervella, Y., et al. (2018). Suspended sediment dynamics in the macrotidal Seine Estuary (France): 1. Numerical modeling of turbidity maximum dynamics. *Journal of Geophysical Research: Oceans*, *123*(1), 558–577. https://doi.org/10.1002/2017JC013185

Hoefel, F. (2003). Wave-induced sediment transport and sandbar migration. *Science*, *299*(5614), 1885–1887. https://doi.org/10.1126/science.1081448

Hu, J., Li, S., & Geng, B. (2011). Modeling the mass flux budgets of water and suspended sediments for the river network and estuary in the Pearl River Delta, China. *Journal of Marine Systems*, *88*(2), 252–266. https://doi.org/10.1016/j.jmarsys.2011.05.002

Huijts, K. M. H., De Swart, H. E., Schramkowski, G. P., & Schuttelaars, H. M. (2011). Transverse structure of tidal and residual flow and sediment concentration in estuaries: Sensitivity to tidal forcing and water depth. *Ocean Dynamics*, *61*(8), 1067–1091. https://doi.org/10.1007/s10236-011-0414-7

Huijts, K. M. H., Schuttelaars, H. M., de Swart, H. E., & Friedrichs, C. T. (2009). Analytical study of the transverse distribution of along-channel and transverse residual flows in tidal estuaries. *Continental Shelf Research*, *29*(1), 89–100. https://doi.org/10.1016/j.csr.2007.09.007

Huijts, K. M. H., Schuttelaars, H. M., de Swart, H. E., & Valle-Levinson, A. (2006). Lateral entrapment of sediment in tidal estuaries: An idealized model study. *Journal of Geophysical Research*, *111*(12). https://doi.org/10.1029/2006JC003615

Jia, L., & Yi, W. (2013). Study of characteristics and transport pattern of surface sediment during dry seasons in Huangmao Estuary (in Chinese). *Journal of Sediment Research*, *1*, 60–66. https://doi.org/10.3969/j.issn.0468-155X.2013.01.010

Kumar, M., Schuttelaars, H. M., & Roos, P. C. (2017). Three-dimensional semi-idealized model for estuarine turbidity maxima in tidally dominated estuaries. *Ocean Modelling*, *113*, 1–21. https://doi.org/10.1016/j.ocemod.2017.03.005

Lerczak, J. A., & Rockwell Geyer, W. (2004). Modeling the lateral circulation in straight, stratified estuaries. *Journal of Physical Oceanography*, *34*(6), 1410–1428. https://doi.org/10.1175/1520-0485(2004)034<1410:MTLCIS>2.0.CO;2

Lerczak, J. A., Geyer, W. R., & Chant, R. J. (2006). Mechanisms driving the time-dependent salt flux in a partially stratified estuary. *Journal of Physical Oceanography*, *36*, 2296–2311.

Li, Y., & Li, M. (2011). Effects of winds on stratification and circulation in a partially mixed estuary. *Journal of Geophysical Research*, *116*(12). https://doi.org/10.1029/2010JC006893

Li, Y., & Li, M. (2012). Wind-driven lateral circulation in a stratified estuary and its effects on the along-channel flow. *Journal of Geophysical Research*, *117*(9). https://doi.org/10.1029/2011JC007829

Meade, R. H. (1969). Landward transport of bottom sediments in estuaries of the Atlantic Coastal Plain. *J. Sediment. Petrol.*, *39*(1), 222–234.

Nunes, R., & Simpson, J. (1985). Axial convergence in a well-mixed estuary. *Estuarine Coastal and Shelf Science*, *20*(5), 637–649. https://doi.org/10.1016/0272-7714(85)90112-X

Ralston, D. K., Geyer, W. R., & Warner, J. C. (2012). Bathymetric controls on sediment transport in the Hudson River estuary: Lateral asymmetry and frontal trapping. *Journal of Geophysical Research*, *117*(10), 1–21. https://doi.org/10.1029/2012JC008124

Saha, S., et al. (2010). The NCEP climate forecast system reanalysis. *Bull. Am. Meteorol. Soc.*, *91*, 1015–1057.

Sanford, L. (1994). Wave-forced resuspension of upper Chesapeake Bay muds. *Estuaries and Coasts*, *17*(1), 148–165. https://doi.org/10.1007/BF02694911

Sanford, L. P., Sellner, K. G., & Breitburg, D. L. (1990). Covariability of dissolved oxygen with physical processes in the summertime Chesapeake Bay. *Journal of Marine Research*, *48*(3), 567–590. https://doi.org/10.1357/002224090784984713

Sassi, M., Duran-Matute, M., van Kessel, T., & Gerkema, T. (2015). Variability of residual fluxes of suspended sediment in a multiple tidal-inlet system: the Dutch Wadden Sea. *Ocean Dynamics*, *65*(9–10), 1321–1333. https://doi.org/10.1007/s10236-015-0866-2

Schulz, K., Endoh, T., & Umlauf, L. (2017). Slope-induced tidal straining: Analysis of rotational effects. *Journal of Geophysical Research: Oceans*, *122*(3), 2069–2089. https://doi.org/10.1002/2016JC012448

Scully, M. E. (2010). Wind modulation of dissolved oxygen in Chesapeake Bay. *Estuaries and Coasts*, *33*(5), 1164–1175. https://doi.org/10.1007/s12237-010-9319-9

Scully, M. E., Friedrichs, C., & Brubaker, J. (2005). Control of estuarine stratification and mixing by wind-induced straining of the estuarine density field. *Estuaries*, *28*(3), 321–326. https://doi.org/10.1007/BF02693915

Scully, M. E., & Friedrichs, C. T. (2007a). Sediment pumping by tidal asymmetry in a partially mixed estuary. *Journal of Geophysical Research*, *112*(7), 1–12. https://doi.org/10.1029/2006JC003784

Scully, M. E., & Friedrichs, C. T. (2007b). The importance of tidal and lateral asymmetries in stratification to residual circulation in partially mixed estuaries. *Journal of Physical Oceanography*, *37*(6), 1496–1511. https://doi.org/10.1175/JPO3071.1

Scully, M. E., Geyer, W. R., & Lerczak, J. A. (2009). The influence of lateral advection on the residual estuarine circulation: A numerical modeling study of the Hudson River estuary. *Journal of Physical Oceanography*, *39*(1), 107–124. https://doi.org/10.1175/2008JPO3952.1

Sommerfield, C. K., & Wong, K.-C. (2011). Mechanisms of sediment flux and turbidity maintenance in the Delaware Estuary. *Journal of Geophysical Research*, *116*(C1), C01005. https://doi.org/10.1029/2010JC006462

Umlauf, L., & Burchard, H. (2003). A generic length-scale equation for geophysical turbulence models. *Journal of Marine Research.*, *61*, 235–265. https://doi.org/10.1357/002224003322005087

Uncles, R. J., Elliott, R. C. A., & Weston, S. A. (1985). Dispersion of salt and suspended sediment in a partially mixed estuary. *Estuaries*, *8*(3), 256–269. https://doi.org/10.1007/BF02803941

Valle-Levinson, A. (2008). Density-driven exchange flow in terms of the Kelvin and Ekman numbers. *Journal of Geophysical Research*, *113*(4), 1–10. https://doi.org/10.1029/2007JC004144

Van Der Wegen, M., Dastgheib, A., Jaffe, B. E., & Roelvink, D. (2011). Bed composition generation for morphodynamic modeling: Case study of San Pablo Bay in California, USA. *Ocean Dynamics*, *61*(2–3), 173–186. https://doi.org/10.1007/s10236-010-0314-2

Warner, J. C., Sherwood, C. R., Signell, R. P., Harris, C. K., & Arango, H. G. (2008). Development of a three-dimensional, regional, coupled wave, current, and sediment-transport model. *Computers and Geosciences*, *34*(10), 1284–1306. https://doi.org/10.1016/j.cageo.2008.02.012

Wei, X., Kumar, M., & Schuttelaars, H. M. (2018). Three-dimensional sediment dynamics in well-mixed estuaries: Importance of the internally generated overtide, spatial settling lag, and gravitational circulation. *Journal of Geophysical Research: Oceans*, *123*, 1062–1090. https://doi.org/10.1002/2017JC012857

Whipple, A. C., Luettich, R. A., Reynolds-Fleming, J. V., & Neve, R. H. (2018). Spatial differences in wind-driven sediment resuspension in a shallow, coastal estuary. *Estuarine, Coastal and Shelf Science*, *213*(August), 49–60. https://doi.org/10.1016/j.ecss.2018.08.005

Willmott, C. J. (1981). On the validation of models. *Physical Geography*, *2*(2), 184–194. https://doi.org/10.1080/02723646.1981.10642213

Xia, X. M., Li, Y., Yang, H., Wu, C. Y., Sing, T. H., & Pong, H. K. (2004). Observations on the size and settling velocity distributions of suspended sediment in the Pearl River Estuary, China. *Continental Shelf Research*, *24*(16), 1809–1826. https://doi.org/10.1016/j.csr.2004.06.009

Xie, X., & Li, M. (2018). Effects of wind straining on estuarine stratification: A combined observational and modeling study. *Journal of Geophysical Research: Oceans*, *123*(4), 2363–2380. https://doi.org/10.1002/2017JC013470

Zhang, G., Cheng, W., Chen, L., Zhang, H., & Gong, W. (2019). Transport of riverine sediment from different outlets in the Pearl River Estuary during the wet season. *Marine Geology*, *415*(March), 105957. https://doi.org/10.1016/j.margeo.2019.06.002

Zhang, W., Ruan, X., Zheng, J., Zhu, Y., & Wu, H. (2010). Long-term change in tidal dynamics and its cause in the Pearl River Delta, China. *Geomorphology*, *120*(3–4), 209–223. https://doi.org/10.1016/j.geomorph.2010.03.031